nature portfolio

https://doi.org/10.1038/s41586-022-04561-z

Supplementary information

Self-regulated non-reciprocal motions in single-material microstructures

In the format provided by the authors and unedited

Supporting Information

Self-regulated non-reciprocal motions in single-material microstructures

Shucong Li[#,1], Michael M. Lerch[#,2,3], James T. Waters[4], Bolei Deng[2], Reese S. Martens[2], Yuxing Yao[1], Do Yoon Kim[2], Katia Bertoldi[2], Alison Grinthal[2], Anna C. Balazs[4], Joanna Aizenberg[*,1,2]

[1] *Department of Chemistry and Chemical Biology, Harvard University, Cambridge, MA 02138;*
[2] *John A. Paulson School of Engineering and Applied Sciences, Harvard University, Cambridge, MA 02138;*
[3] *Stratingh Institute for Chemistry, University of Groningen, Groningen, 9747 AG, The Netherlands*
[4] *Chemical Engineering Department, University of Pittsburgh, Pittsburgh, PA 15261;*
[#] *Contributed equally*

Corresponding Author:
** jaiz@seas.harvard.edu*

This Supplementary Information includes:

Materials and Methods

Theoretical Models 1 to 3

Supplementary Results & Figures 1 to 35

Captions for Supplementary Videos 1 to 10

Further Supplementary Materials:

Supplementary Videos 1 to 10 (.mp4)

Table of Contents

1 Materials and Methods

1.1 Materials

General reagent information: For the preparation of commercially unavailable compounds, unless stated otherwise, all reactions were carried out in oven- and flame-dried glassware using standard Schlenk techniques and were run under argon atmosphere. The reaction progress was monitored by Thin-layer chromatography (TLC). Starting materials, reagents and solvents were purchased from *MilliporeSigma, Honeywell, J.T. Baker, Macron, Fischer,* or *Acros* and were used as received, unless stated otherwise. Solvents for the reactions were of quality puriss., p.a. Anhydrous solvents were purchased in septum-sealed bottles over molecular sieves. Deuterated solvents were purchased from *Cambridge Isotope Laboratories, Inc*. For aqueous solutions, deionized MilliQ water was used. 2,5-dihydroxybenzoic acid, benzyl bromide, 4-butyloxybenzoic acid, 4-hydroxybutyl acrylate, 4-pyrrolidinopyridine, *N*,*N'*-dicyclohexylcarbodiimide (DCC), fluorescein, palladium on carbon (10 w%, matrix activated), sodium bicarbonate ($NaHCO_3$), trichloro(*1H*,*1H*,*2H*,*2H*-perfluorooctyl) silane, and silica gel (Davisil Grade 633, high-purity grade, pore size 60 Å, 200-425 mesh particle size) were purchased from *MilliporeSigma*. Methacryloxyethyl thiocarbamoyl rhodamine B dye was purchased from *Polysciences, Inc*.

General considerations: Thin-layer chromatography analyses were performed on commercial Kieselgel 60 F_{254} silica gel plates with fluorescence-indicator UV_{254} (*Merck*, TLC silica gel *60 F_{254}*). For detection of components, UV light at λ = 254 nm or λ = 365 nm was used. Alternatively, oxidative staining using aqueous basic potassium permanganate solution ($KMnO_4$), aqueous cerium phosphomolybdic acid solution (Seebach's stain[1]), or iodine stain were used. Drying of solutions was performed with $MgSO_4$ and volatiles were removed with a rotary evaporator.

General analytical information: Nuclear Magnetic Resonance spectra were measured at the Harvard University Laukien-Purcell Instrumentation Center with a Varian Unity/Inova 500 spectrometer (500 MHz). All spectra were measured at room temperature (22–24 °C). Chemical shifts for ^{1}H-NMR spectra were reported relative to the residual solvent peak [in ppm; $CDCl_3$: δ_H = 7.26][2]. The multiplicities of the signals are denoted by *s* (singlet), *d* (doublet), *t* (triplet), *q* (quartet), and *m* (multiplet).

Liquid crystalline elastomer constituents: Liquid crystal mesogen **1** was synthesized according to an established literature procedure[3]. The photoswitchable crosslinker (**2**, 4,4'-bis(9-acryloyloxynonyloxy) azobenzene) was purchased from *Synthon Chemicals* (ST04181). Photoinitiator IRGACURE® 819 (bis(2,4,6-trimethylbenzoyl)-phenylphosphineoxide) was purchased from *Ciba Specialty Chemical Inc*.

Microstructure fabrication: 4'' Silicon wafers and 6'' silicon-dioxide carriers were purchased from *Nova Electronic Materials*. Photoresist SPR220-7.0 was purchased from *Microchem*. Sylgard® 184 silicone kit was purchased from *Ellsworth Adhesive Systems* and used at a ratio 10:1 wt/wt Sylgard® base to curing agent. Cover glass (22 mm in diameter, 0.21 mm in thickness), microscopy glass slides (25 x 75 mm, 1 mm in thickness) and polyimide (Kapton®) tape were obtained from *VWR*. The high-temperature neodymium magnets (NdFeB, Grade N42SH; 1" x 1/2" x 1/2"; BX088SH) were purchased from *K&J Magnetics, Inc*. The magnetic field strength on the magnet was measured with a DC Gaussmeter (Model GM-1-ST) obtained from *AlphaLab Inc*.

UV-polymerization: A Dymax 2000-EC UV Curing Flood lamp with chamber (light intensity of ~18 mW/cm^2) with a custom-made steel mesh (Gerard Daniel Worldwide, Inc., SST 304 TW, mesh .007, as neutral density filter) was used to initiate polymerization.

1.2 Methods

1.2.1 Materials Characterization

Differential Scanning Calorimetry (DSC) was performed on a Thermal Analysis (TA) DSC Q200 instrument. The program for monomer mixtures consisted of two cycles from –5 °C to 120 °C and back with a 10 °C/min rate. The program for the liquid crystalline elastomer consisted of two cycles from –5 °C to 200 °C and back with a 10 °C/min rate.

Scanning electron microscopy of the Si master and 'frozen' deformed LCE microstructures was performed on a Zeiss Supra55VP Field Emission Scanning Electron Microscope (FESEM). For experimental reasons, the SEM and the confocal images are not from exactly the same posts but from posts having the same director alignment.

Confocal Laser Scanning Microscopy (LSM) measurements were performed on a Zeiss LSM 700 instrument with 5X, 10X and 40X objectives and a custom-made sample holder to control the temperature across the LCE microstructured sample. For fluorescence read-out, LCE microstructures were coated with a solution of the dye methacryloxyethyl thiocarbamoyl rhodamine B in ethanol, that was applied dropwise to the sample and left evaporating. The fluorescent dye was excited with a λ_{ex} = 555 nm laser during measurements. For directional photoactuation with a 365 nm UV LED (Thorlabs M365F1), the microstructures were heated to 60°C (above their glassy state, T_g ~45°C) and deformation trajectories were followed as time-series and by adjusting the focal plane as the posts deformed. The time-series were subsequently image-tracked using a MATLAB script. Confocal images of *i/iv* and *ii/iii* in Manuscript Figure **2** were taken from two different microposts having the same director alignment. For water-immersion, fluorescein dye (excited with λ_{ex} = 488 nm) was used. Z-stack and time series data were analyzed with the Zeiss ZEN black software.

For UV-irradiations, an LED mounted in a heatsink (Thorlabs, M365F1) was used and controlled with a T-cube driver (Thorlabs, LEDD1B) for continuous adjustment of light-intensity. Twelve levels of intensity were used: (1) 1.0 mW/cm^2, (2) 2.5 mW/cm^2, (3) 4.8 mW/cm^2, (4) 9.0 mW/cm^2, (5) 12.6 mW/cm^2, (6) 15.8 mW/cm^2, (7) 24.8 mW/cm^2, (8) 42.1 mW/cm^2, (9) 66.2 mW/cm^2, (10) 90.0 mW/cm^2, (11) 103.8 mW/cm^2, and (12) 115.0 mW/cm^2. Irradiance levels were determined at 1 cm distance from the light-source with a power meter (Thorlabs, S310C in conjunction with PM100D). For irradiation in intervals, a Transistor Transistor Logic (TTL) signal provided by an Arduino Uno controller was used to switch on or off the LED through the Trigger Mode of the T-cube driver.

UV-visible spectra were obtained on an Agilent 8453 UV-vis diode array spectrophotometer equipped with a Peltier-based temperature-controlled cuvette holder. Samples were prepared with Uvasol®-grade solvents and measured in quartz cuvettes of 10 mm pathlength. The obtained UV/vis spectra were baseline corrected. Data-analysis was performed using R (*https://www.r-project.org/*), GraphPad Prism, or Spectragryph software. Photoswitching of crosslinker **2** in dichloromethane solution was performed with an LED M365F1 (Thorlabs) at room temperature. Spectra for photoswitching within a polymeric thin film (non-aligned LCE, with 7.5 wt% compound **2** as crosslinkers) were collected at 60 °C by immersing the polymer film in quartz cuvettes filled with water upon irradiation with LED M365FP1 (Thorlabs).

To monitor photothermal heating, a thermal IR camera (FLIR, A8303sc, InSb detector, 3.0–5.0 µm spectral range, 1280x720 resolution, f/4.0, GigE/CXP 60Hz) with a 4X microscope lens objective (FLIR, 50 mm lens) was used. Time-series were analyzed with ResearchIR software. The IR camera was placed on a boom tripod and suspended above the sample for imaging. The

sample was placed on a heating element at 60 °C on a lab jack (Thorlabs, L490) for focus adjustment.

1.2.2 Image Tracking

The positions and rotations of the LCE microposts were tracked based on experimental videos by fluorescent confocal microscopy using MATLAB (Supplementary Figure **12**). The image tracking process takes three steps in MATLAB:

(1) Experimental videos were converted to image sequences, where each frame corresponds to an image;

(2) For each image, a color threshold was first set to convert the image into a binary plot, where the pixels inside the post have a value of 1 and pixels outside the post have a value of 0. Then the boundary of the considered micropost was extracted for each binary figure using the MATLAB function 'bwboundaries';

(3) Finally, the boundary of the micropost was fit by a square using linear regression, in which the residue function is defined by the summation of distances between the post boundary and the fitting square. The fitted square contains information about the position and rotation of the micropost at every time point.

1.2.3 Synthesis and Characterization of the Liquid Crystalline Elastomer (LCE) Monomer

Synthesis: Following a previously published procedure by Ratna and co-workers[3], side-on LC monomer **1** ((4″-acryloyloxybutyl) 2,5-di(4′-butyloxybenzoyloxy)benzoate) was synthesized in four steps from commercially available starting materials (Supplementary Figure **2**). Spectral properties matched previously reported values: ^{1}H-NMR (500 MHz, $CDCl_3$) δ (ppm): 1.00 (*t*, *J* = 7.4, 2.6 Hz, 6H), 1.46–1.68 (m, 8H), 1.75–1.86 (m, 4H), 3.95–4.09 (m, 6H), 4.20 (*t*, *J* = 6.0 Hz, 2H), 5.77–5.82 (m, 1H), 6.03–6.12 (m, 1H), 6.32–6.40 (m, 1H), 6.92–7.02 (m, 4H), 7.26–7.28 (m, 1H), 7.43–7.48 (m, 1H), 7.89 (s, 1H), 8.10–8.19 (m, 4H).

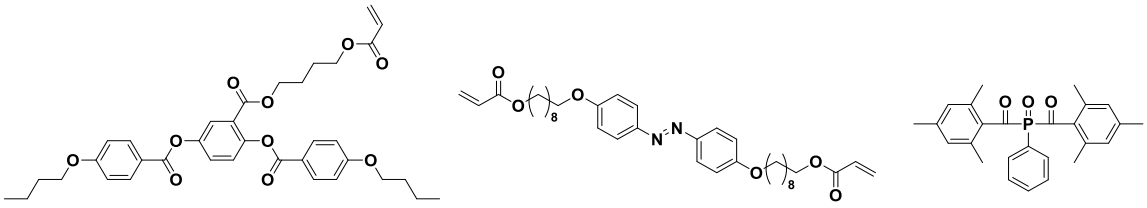

1 LCE monomer

2 Azobenzene crosslinker

Irgacure 819

Preparation of LC monomer mixture: 90.5 mg of side-on monomer **1**, 7.5 mg of photoresponsive crosslinker **2**, and 2 mg of IRGACURE® 819 were dissolved in roughly 0.5–1 mL of anhydrous dichloromethane in a vial, mixed thoroughly, and applied dropwise to a cleaned microscopy glass slide (washed sequentially with water, acetone, and 2-propanol, then blow-dried under nitrogen flow). The solvent was allowed to slowly evaporate overnight in the dark to yield the crystallized LC monomer mixture. The amounts correspond to 7.7 mol% (crosslinker **2**) and 3.0 mol% (photoinitiator). The crystallized LC monomer mixture on the glass slide can be conveniently scratched off onto the hot PDMS mold during the next fabrication step.

1.2.4 Fabrication of LCE Microstructures

Fabrication of the microstructured silicon master: The microstructured silicon master was produced by photolithography followed by reactive ion etching (RIE) at the Center for Nanoscale Systems (CNS) at Harvard University. Photoresist (SPR220-7.0) patterning was performed by UV exposure at 375 nm (470 mJ/cm^2) with a Heidelberg MLA150 Maskless Aligner, held overnight (or at least for 2 h), and developed in CD-26 developer (2 min x 2 times, MICROPOST® MF®), which later served as the mask for the anisotropic etching of the Si wafer substrate using the SPTS Technologies Rapier DRIE System (Model Omega LPX Rapier), to obtain the array of Si microstructures. The geometry and size of the structures fabricated for this study are shown in Supplementary Figure **1**. For a height of 150 µm two rounds of subsequent etching runs (2 x 75 µm) were required. The 3D structure of the Si microposts was characterized by scanning electron microscopy (Zeiss Supra 55 VP Field Emission Scanning Electron Microscope, FESEM).

Fabrication of the molds for LCE microstructures[4,5]**:** After removal of the remaining photoresist with oxygen plasma (PlasmaEtch, PE-200, 300W, 20 min), the Si microstructure array was functionalized with trichloro(*1H*,*1H*,*2H*,*2H*-perfluorooctyl) silane to render the microstructures hydrophobic. Subsequently, a PDMS negative replica of the microstructured surface was generated by pouring the well-mixed (using a Thinky Mixer ARE-310, Thinky U.S.A., Inc.) polydimethylsiloxane (PDMS) precursor (mixture of Sylgard® 184 base and crosslinker at a ratio of 10:1 *wt*:*wt*) on top of the Si wafer, degassing and curing at 70 °C for 2 h. Finally, the PDMS was carefully peeled off from the Si wafer and used as a negative mold for the synthesis of LCE microstructures.

Synthesis of LCE microstructures: The crystallized monomer mixture (~20 mg) was scratched from the prepared glass slide onto the PDMS mold and molten into molding cavities. The mold was then covered with a microscopy glass coverslip (held in place by Kapton®-tape) and placed oriented in a magnetic field generated by the desired geometric assembly of NdFeB-based magnets with a surface field of approximately 0.5 T to align the LC mesogens in an arbitrary direction relative to the microstructures' principal axes (Supplementary Figure **3a**). When the sample had reached 80 °C (isotropic phase), the setup was slowly cooled down to 60 °C at a rate of 1 °C/min, and then polymerized under UV irradiation (Dymax 2000-EC UV Curing Flood Lamp System with a custom metal mesh reducing light intensity to ~18 mW/cm^2)[6] under inert atmosphere (N_2) for 1 h. To keep the azobenzene moiety from photoisomerizing (disruption of alignment) and possible photodegradation during UV-polymerization, an optical cut-off filter (Newport FSQ-GG400) was used, that blocks any light with wavelength shorter than 400 nm. After ~1 h of polymerization, the sample with the encrypted nematic director orientation was cooled down to room temperature and the PDMS mold was carefully peeled off from the LCE microstructures on the glass coverslip.

Synthesis of the LCE thin film for UV-Visible measurements: We applied ~10 mg of the reactive monomer mixture onto a flat rectangular PDMS slab on a hot plate at 80 °C (isotropic phase) and placed two 6 µm plastic spacers at the two ends of the PDMS slab. We then covered the molten mixtures with a microscopy glass coverslip (held in place by Kapton®-tape). Cooling and polymerization of the thin film were conducted under the same conditions as for the LCE microstructure described above. After ~1 h of polymerization, the sample was cooled down to room temperature and the PDMS mold and spacers were carefully removed leaving the thin film attached on the coverslip. The coverslip was later cut into a narrow piece to be able to fit into the quartz cuvettes of 10 mm path length for the UV-Vis measurements.

1.2.5 Fabrication of Freestanding Jointed LCE Microstructures

Freestanding jointed LCE microstructures (V- and X-shape) were synthesized following a procedure resembling the one described in SI section 1.2.4 (Supplementary Figure **32**). Instead of a glass coverslip, however, a thin PDMS slab was used as cover to avoid surface attachment (less adhesion) of the polymerized LCE structure. After placing the flat PDMS slab onto the negative PDMS mold filled with the LC mixture melt, gentle pressure was applied to enhance contact between the two PDMS layers as well as to remove any excess LC mixture. In addition, a trace amount of oxygen (from air) in the PDMS mold helps to suppress polymerization at the PDMS-PDMS interface and therefore to avoid formation of a thin LCE layer in between. The same magnet, alignment, and polymerization setup as described in SI section 1.2.4 (Supplementary Figure **3a**) were used to yield polymerized LCE microstructures with jointed shape. Upon polymerization, stretching and squeezing the flexible PDMS mold helps to release the LCE microstructure. Custom-made capillary tubes (the thin end has a diameter of ~10 µm) were used to pick up the released freestanding LCE microstructures and fix certain spots for further UV actuation and microscopy imaging. Note that for structures in which a thin LCE layer remains, this thin substrate layer could in principle also (undesirably) influence the overall jointed microstructure deformation. The described procedure avoids formation of such a film as much as possible.

1.2.6 Comment on the mechanism of magnetic alignment

The propensity of monomer **1** ((4″-acryloyloxybutyl) 2,5-di(4′-butyloxybenzoyloxy)benzoate), a type of calamitic LC mesogen, to align within a magnetic field is well-established[3,7,8]. Calamitic LCs are often diamagnetic due to a zero-net spin and the dispersed electron distribution associated with the delocalized charge, for example, from phenyl rings in the mesogen structure. When placed in a magnetic field, the ring currents associated with these aromatic units induce a magnetic moment perpendicular to the conjugated aromatic ring plane in opposition to the applied magnetic field, which thereby raises the free energy. The density of free energy g_{mag} in LC mesogens in a magnetic field can be expressed as[9]:

$$g_{mag} = g_0 - \frac{1}{2}\mu_0^{-1}B^2\chi_\perp - \frac{1}{2}\mu_0^{-1}\Delta\chi(\mathbf{B}\cdot\mathbf{n})^2$$

where $\Delta\chi = \chi_\parallel - \chi_\perp$, with $\chi_\parallel$ and $\chi_\perp$ being the magnetic susceptibilities parallel and perpendicular to the LC mesogen principal axis, respectively. μ_0 denotes the permeability of free space, and $\mathbf{B}$ refers to the magnetic field and $\mathbf{n}$ is the director. For most calamitic LCs, both $\chi_\parallel$ and $\chi_\perp$ are negative but the delocalized electron density makes a major contribution to $\chi_\perp$ resulting in $|\chi_\perp| > |\chi_\parallel|$ and $\Delta\chi$ positive. Therefore, in order to minimize the free energy, the director $\mathbf{n}$ will align parallel to the magnetic field $\mathbf{B}$[9] (Supplementary Figure **3b**). In our research, we use an externally applied weak magnetic field (~0.5 T) to orient mesogens uniaxially within the molded LCE precursor mixture in an arbitrary direction in 3D by simply changing the orientation of the mold within the static magnetic field. Polymerization locks in this uniaxial nematic director orientation within the resulting microstructures. (Note that magnetic field is only used during the fabrication and not in subsequent actuation process.)

2 Supplementary Models

2.1 Model 1: Finite Element Simulation

To obtain a detailed description of the evolution of the shape deformation, twisting, and deflection of the post, and how these properties relate to the propagating isomerization front, we implemented a finite element model to simulate the behavior of the micropost in response to light at different intensities and illumination directions, for different orientations of the nematic director.

The material is discretized into a set of hexahedral (initially cubic) finite elements, each bounded by eight nodes. The evolution of the mesh in time is dictated by the free energy of the system, summed over all of the finite elements constituting the post. This free energy can be differentiated with respect to the nodal coordinates to update the dynamics of the system at each time step[6,10]. This free energy is given as

$$F = \frac{\kappa}{2}\log^2 J - \frac{\mu(I_m-3)}{2}\log\left(\frac{I_m-I_1}{I_m-3}\right) + \alpha\,\Delta S\,Q_{ij}\epsilon_{ij} \qquad \text{(S1)}$$

where the first and second terms describe the resistance of the material to bulk and shear deformations, respectively. κ is the bulk modulus of the material, taken to be 28 MPa, and μ is the shear modulus, taken to be 570 KPa, as used in earlier numerical studies[6,10]. I_1 and J are the first invariant and square root of the third invariant of the strain tensor ϵ_{ij}, and I_m is a limiting extension of polymer chains within the material, here taken to be 30. The third term describes the tendency of the material to deform brought on by changes in the polymer chain conformations as the system moves from the nematic to the isotropic state. In this term, the coupling coefficient α was fit as 0.175 μ in a prior study[6,10]. Q_{ij} is the traceless nematic tensor, assumed to be fixed in the frame of the material.

In our numerical model, the change in nematic order ΔS in this third term is negative and assumed to be proportional to the fraction of the azobenzenes in the *cis*-state. Using the theoretical model of Warner and co-workers[11], the isomerization of the photoswitches in the material is evolved in time at each location in the mesh, as a function of the incident light intensity:

$$\frac{\partial n_t}{\partial t} = -\Gamma I n_t + (1-n_t)/\tau\ . \qquad \text{(S2)}$$

Here n_t represents the fraction of the system in the *trans*-state, which must sum to one with the *cis*-fraction n_c.

The first term on the right-hand side in the above equation corresponds to the excitation of *trans*-isomers, and depends on the fraction of remaining *trans*-isomers and the incident light intensity I. The constant Γ determines the *trans*-to-*cis* transition rate and chosen to have a value of 10^{-5} s^2/Kg to match the experimentally observed response at low and high intensities. The second term describes the relaxation of *cis*-isomers back to the *trans*-state which is dictated by a relaxation time τ, here taken to be 120 s, corresponding to the experimentally observed timescale of minutes. This time evolution is solved at each node in the mesh at each time step of the simulation. To obtain the incident light intensity, we perform a ray-tracing algorithm through the elements of the mesh to each node. An attenuation length λ_j is calculated for each element j, based on the isomerized fraction n_t at each node i comprising the element:

$$\lambda_j = \frac{\gamma\Gamma}{8}\sum_{i=1}^{8} n_t^i\ . \qquad \text{(S3)}$$

The constant γ, representing the number density of chromophores and the energy of each transition, is set to a value of 2×10^{10} Kg/ms^2 to reproduce the appropriate Beer length ($l_B = 1/\gamma\Gamma$ = 5 μm) at low intensities. For light incident along a vector $\hat{\boldsymbol{v}}_{\boldsymbol{l}}$ and a mesh node i located at $\boldsymbol{r}_{\boldsymbol{i}}$, we can check each of the elements containing node i for a face consisting of four points $\boldsymbol{r}_{\boldsymbol{j}}$ ($j = 1,2,3,4$) such that a ray parallel to $\hat{\boldsymbol{v}}_{\boldsymbol{l}}$ intersecting the face can reach $\boldsymbol{r}_{\boldsymbol{i}}$. This is equivalent to solving the equation

$$\boldsymbol{r}_{\boldsymbol{i}} = l_B \hat{\boldsymbol{v}}_{\boldsymbol{l}} + \sum_{j=1}^{4} \alpha_j \boldsymbol{r}_j \qquad \text{(S4)}$$

where the α_j coefficients are the finite element shape functions evaluated on the face of the element. These coefficients are nonnegative and sum to unity, and the path length l_B must be greater than zero. The value of these shape functions at the point of intersection will give us the weights to assign to each of the intensities when relating them to the intensity at the point of interest. The quantity l_B is the path length through the element to the node i along the incident light vector, allowing us to write the intensity at $\boldsymbol{r}_{\boldsymbol{i}}$ as a function of these quantities, the intensity at other nodes, and the local attenuation length λ for the element in question:

$$I_i = e^{-\lambda l_B} \sum_{j=1}^{4} \alpha_j I_j \ . \qquad \text{(S5)}$$

Mesh nodes that lie on a surface of the post directly exposed to the light will be assigned an intensity I_0, equal to that at the light source. Additional relations of the same form as S5 may be necessary if there are nodes and faces satisfying equation S4 but belonging to different elements—such a case would correspond to light passing through the material for some distance, passing outside the material, and then striking the surface of the post again, and is possible if the post deforms into a nonconvex shape. In this instance, the attenuation per length of light outside of the micropost is assumed to be negligible.

This will give a system of linear equations that can then be solved to obtain the intensity at each node in the finite element mesh. This is used to update the isomerized fraction, which in turn is used to update the accelerations of the mesh nodes and the attenuation length through each mesh element, which will be used to compute the intensities for subsequent time steps.

The above methodology can then be extended to arrays of posts, with equation S4 used to trace light rays through one structure and into another disconnected structure and determine what parts of the surface of each post will be obscured by neighboring posts. Such simulations predict interactions within arrays of posts similar to what was observed experimentally (Supplementary Figure **27**, Video **6**). We find that for a row of posts, we can approximate the effect of a finite-size light source in experiment with two ideal light sources (assumed to be propagating from infinity along all vectors parallel to $\hat{\boldsymbol{v}}_{\boldsymbol{l}}$) separated at an angle of ±1° from the post-to-post separation axis. The first post on the path of the incident light bends towards the light as it would in isolation. However, the second post is subject only to glancing incidence on its sides—it is unstable in the sense that a slight deflection out of the plane defined by the vertical axes of the posts and the line connecting the post bases will lead to more isomerization on that face. This will induce more contraction and further deflection out of the plane. The direction of this out-of-plane deflection of the second post will cause selective irradiation of the next (third) post from any glancing incidence but not the other. This causes the third post in the sequence to deflect out of plane in the opposite direction. This out-of-plane deflection will in turn change irradiation of the subsequent post, and the effect will propagate along the line of posts.

2.2 Model 2: Theoretical Model[12] for Nonlinearity in 'Light-seeking' and 'Light-avoiding' Behavior

Let us consider the LCE molecules with the director θ away from Z axis in the YZ plane. When actuated, the molecular alignment induces a contraction with a strain $-\varepsilon_a$ along the LCE director. Furthermore, due to the Poisson effect (as the material keeps constant volume), the material expands perpendicular to its alignment by $\varepsilon_a/2$ (Supplementary Figure **15a**). To facilitate our analysis, we decompose the strain state in the Y-Z axes and represent the strain state by normal strain ε_{yy}, ε_{zz} and shear strain τ_{yz} (Supplementary Figure **15a**):

$$\begin{aligned} \varepsilon_{yy} &= -\frac{\varepsilon_a}{4} + \frac{3\varepsilon_a}{4}\cos(2\theta) \\ \varepsilon_{zz} &= -\frac{\varepsilon_a}{4} - \frac{3\varepsilon_a}{4}\cos(2\theta) \\ \tau_{yz} &= \frac{3\varepsilon_a}{4}\sin(2\theta)\ . \end{aligned} \qquad \text{(S6)}$$

For the studied micropost, we denote its height as h and edge length as a. As the UV light activates the material only within the thickness l_B (penetration depth), the activated part deforms with the strain state described by ε_{yy}, ε_{zz} and τ_{yz}. Such deformation can be approximated as two separate parts, a shear component with strain τ_{yz} and a shortening component in Z-direction with strain ε_{zz} (Supplementary Figure **15b**), resulting in shearing and bending deformation modes, respectively. Note that any deformation in Y-direction is assumed to have no effect on the final configuration of the post. The total deformation of the micropost can be calculated as the sum of these two deformation modes (Supplementary Figure **15c**), *i.e*, (i) shearing and (ii) bending due to the shortening of the activated part.

(i) For the shear deformation, the total tip displacement can be approximated by

$$y_1 = \tau_{yz}\frac{d}{a}h = \frac{3hl_B\varepsilon_a}{4a}\sin(2\theta). \qquad \text{(S7)}$$

(ii) The bending deformation part is much more complex. As we combine the shortened 'activated' part (shortened by $\Delta h = \varepsilon_{zz}h$) with the original part, due to the mismatch between the two parts, the final configuration bends. Furthermore, due to the interaction between the two parts, both parts not only bend but also stretch/compress axially. We set the length of the 'activated' part to h_1 and the 'passive' part to h_2. The balance of force in the axial direction gives,

$$F = Ea(a - l_B)\frac{h-h_2}{h} = Eal_B\frac{h_1-h+\Delta h}{h}. \qquad \text{(S8)}$$

The compatible requirement between the bending and elongation of the beams gives geometrical constraint

$$\frac{a}{2}\beta = h_2 - h_1 \qquad \text{(S9)}$$

where β is the radian of the bent beam. The moment generated by the eccentric forces inside each beam should balance the moment due to the bending of the beams. Therefore,

$$F\frac{a}{2} = \frac{EI\beta}{h} \qquad \text{(S10)}$$

where $I = \frac{1}{12}a^4$ is the moment of inertia of the beam cross-section. Combining equations S8–S10, one can solve for h_1 and h_2, giving

$$h_1 = h - \Delta h + \frac{\Delta h}{\frac{h}{h-\Delta h}\left(\frac{6l_B}{a}+\frac{l_B}{a-l_B}\right)+1}, \text{ and } h_2 = \frac{ah-d(h_1+\Delta h)}{a-l_B}. \quad \text{(S11)}$$

The distance traveled by the tip due to this deformation mode is expressed as

$$y_2 = \frac{h\beta}{2} = \frac{h(h_2-h_1)}{a}. \quad \text{(S12)}$$

The total distance travelled by the post top is then the combined contribution of both deformation modes

$$y = y_1 \pm y_2. \quad \text{(S13)}$$

For the 'light seeking' case, equation S13 takes "+" sign; for the light avoiding case, equation S13 takes "–" sign.

In Supplementary Figure **16** we plot the distance traveled by the post top y as a function of penetration depth l_B for both light seeking and light avoiding cases with different post edge length a and director angle θ.

2.3 Model 3: Simplified Discrete Model for Micropost Arrays

To capture the collective response of a micropost array to irradiation, we establish a simple discrete model. We consider an array of cylindrical posts with diameter a that are exposed to UV light forming an angle β with Y-axis. Because the spot size of the UV light is comparable to its distance from the micropost array, we assume that the shadow formed by a cylindrical post has a long triangular shape and is characterized by its length L_{shadow} (Supplementary Figure **26a**). Note that L_{shadow} depends on many factors, for instance, the distance, spot size and collimation of the UV light, therefore in our model we treat L_{shadow} as a fitting parameter to part of the experimental measurements.

When the array of microposts is exposed to UV light, every microstructure generates a triangular shadow whose direction is determined by light angle β. For each post, we can loop over all other posts to figure out which part of the microstructure is being shadowed by others. For the parts that are not being shadowed, the UV light penetrates l_B into the post and activates certain areas of the post (Supplementary Figure **26b**). Note that since the microposts considered in our study have a thin skin layer that does not respond to UV light, in our model the outer ring with thickness δ_{non} is also not activated. To model the equivalent bending force generated by the illuminated areas S_{light}, we introduce a local coordinate x' and y' that is aligned with the light direction. The equivalent force on the post is therefore calculated as

$$F_{light}^{x'} = \int_{S_{light}} P_{light}\, x' dS_{light} \quad \text{(S14)}$$

$$F_{light}^{y'} = \int_{S_{light}} P_{light}\, y' dS_{light} \quad \text{(S15)}$$

where P_{light} is another fitting parameter characterizing how strong the posts respond to the UV light. For the sake of simplicity, we use the vector $\vec{F}_{light}$ to denote this force.

Furthermore, since the microposts are 3D objects, their shadows are also in 3D. To address this point, we discretize the post as a stack of N disks (Supplementary Figure **26c**). We simply assume that upon activation the post deforms linearly as a tilted straight line. Then the light-induced force is calculated depending on the positions of posts at each layer i, as $\vec{F}_{light}^{i}$. Compared to the disks on the top, disks near the bottom have a larger effect on the positions of the post tip. Therefore, the total equivalent force is defined as $\vec{F}_{light}^{total} = \frac{1}{N}\sum_{i=1}^{N}\frac{N-i-1}{N}\vec{F}_{light}^{i}$. Finally, we use two linear springs k_x and k_y to model the elastic resistance of the posts during bending (Supplementary Figure **26d**). The balance between the light-induced force and the linear springs yields the final positions of the post tips,

$$k_x u = \vec{F}_{light,x}^{total} \text{ and } k_y v = \vec{F}_{light,y}^{total} \qquad \text{(S16)}$$

where u and v are the *x* and *y*-displacements of the post tip. Equation S16 is solved numerically for different post distributions and light directions using the Runge-Kutta method with MATLAB.

3 Supplementary Figures

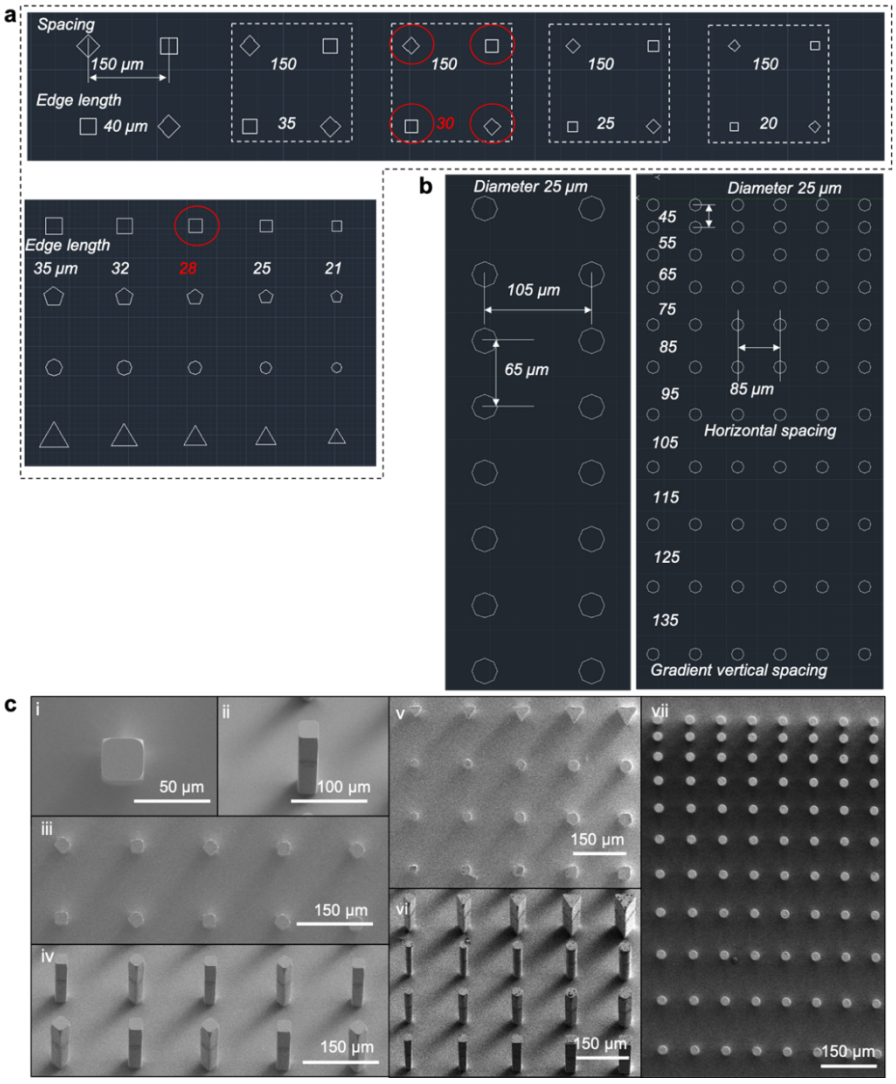

Supplementary Figure 1 | a. Depiction of AutoCAD files used for photolithography on Si wafers. Note the two existing surface designs: one comprising a square/diamond pattern and one including multiple geometries (squares, pentagons, circles, and triangles). Both designs include a gradual change of edge lengths to explore the influence of micropost dimensions on bending/flexural stiffness and deformation behavior. A constant interpost spacing of 150 µm was chosen across the array to avoid potential shadowing from neighbors. Squares with an edge length of 28 µm and 30 µm (red circles) were found to represent a good compromise between mechanical flexibility and quality of magnetic alignment. Square geometry allows for clear visual identification of distinct deformations linked to different illuminated faces of the micropost. **b.** Furthermore, we designed closely packed multipost arrays with uniform (left) or gradient (right) interpost spacing to study post communication effects for collective deformation pattern formation. **c.** Close-up field emission scanning electron microscopy (FESEM, Zeiss Supra 55 VP) images of Si microstructures: a single square micropost of 30 µm side length (i) top- and (ii) sideview; the square/diamond pattern (iii) top- and (iv) side-view; the multiple geometry design (v) top- and (vi) sideview; and (vii) the top-view of the multipost array with gradient interpost spacing. All microstructures are 150 µm in height (calculated from the SEM tilted-view image).

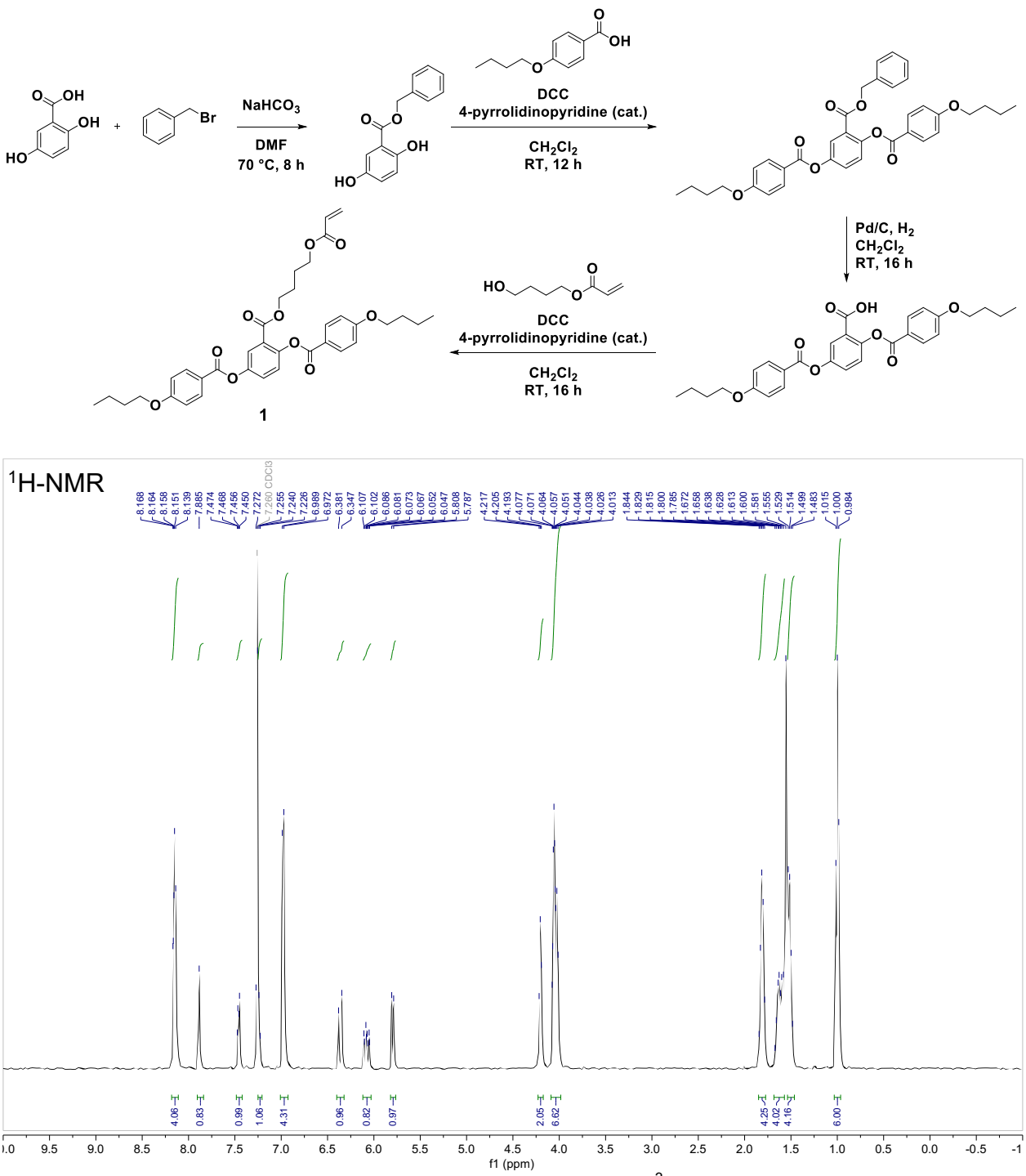

Supplementary Figure 2 | Literature-based synthetic route[3] to side-on liquid crystalline (LC) monomer **1** ((4″-acryloyloxybutyl) 2,5-di(4′-butyloxybenzoyloxy)benzoate). For details on the synthesis, please refer to SI section 1.2.3. The ^{1}H-NMR spectrum of compound **1** in deuterated chloroform is included. Please also refer to our previously reported work[6].

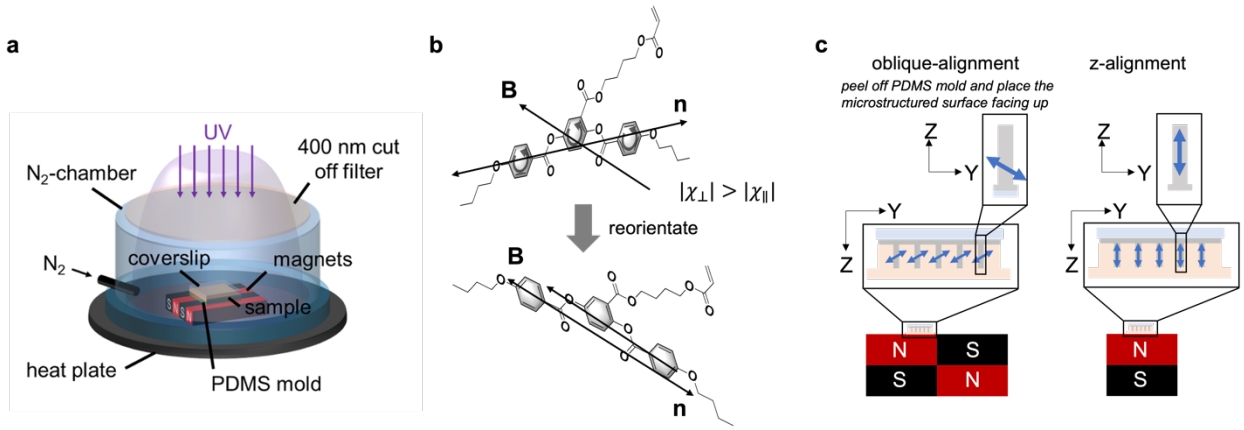

Supplementary Figure 3 | a. Schematic depiction of the experimental setup for the synthesis of microstructured LCE surfaces: a custom-built inert atmosphere chamber with a 400 nm optical cut-off filter (Newport FSQ-GG400) was placed on a conventional hotplate into a UV-curing chamber (Dymax 2000-EC). Commercially available permanent magnets (~ 0.5 T, K&J Magnetics BX088SH) were placed directly on the heating plate, followed by the PDMS negative mold, the LCE monomer mixture, and a coverslip (all held in place by Kapton®-tape). For more details, please refer to SI section 1.2.4. **b.** Diamagnetism and alignment of calamitic mesogen **1** ((4″-acryloyloxybutyl) 2,5-di(4′-butyloxybenzoyloxy)benzoate) in an applied magnetic field **B**. $\chi_{\parallel}$ and $\chi_{\perp}$ are the magnetic susceptibilities parallel and perpendicular to the LC mesogens principal axis, respectively. **n** denotes the LC director orientation. **c.** Schematic depiction of the arrangement of magnets and the LC-melt-filled PDMS mold to achieve an oblique alignment of the LC mesogens (corresponding to the case shown in Manuscript Figure **2** and Supplementary Figure **10**) and z-alignment of LC mesogens (Supplementary Figure **8**). PDMS and the coverslip are not shown in the schematic. To program molecular anisotropy oblique to the microstructure's principal axis, we first chose a director orientation of around the midpoint of 0° and 90° with respect to the Z-axis of the square micropost in the YZ-plane (indicated by the blue double arrow) as one would expect here the most pronounced tilting deformation upon the bulk order-to-disorder phase transition. (Note that magnetic field is only used during the fabrication and not in subsequent actuation process.) For quantitative calculation of the mesogen director orientation inside the microstructures, refer to the COMSOL Multiphysics methods that we previously reported[6].

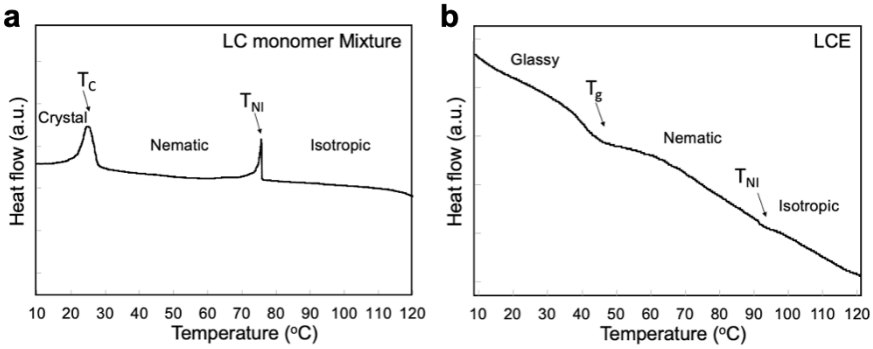

Supplementary Figure 4 | a. Phase behavior of the LC monomer mixture (prepared as described in SI section 1.2.3) measured by differential scanning calorimetry depicting the 2nd cooling cycle from 120 °C to –5 °C at 10 °C/min. The LC monomer mixture exhibits a nematic-to-isotropic phase transition temperature (T_{NI}) of 78 °C and a crystallization temperature (T_C) at 24 °C. **b.** Phase behavior of the UV-polymerized LCE (synthesized as described in SI section 1.2.4) measured by differential scanning calorimetry depicting the 2nd heating cycle from -5 °C to 200 °C at 10 °C/min. The LCE showed a glass transition temperature (T_g) of ~45 °C and a nematic-to-isotropic phase transition temperature (T_{NI}) of ~92 °C.

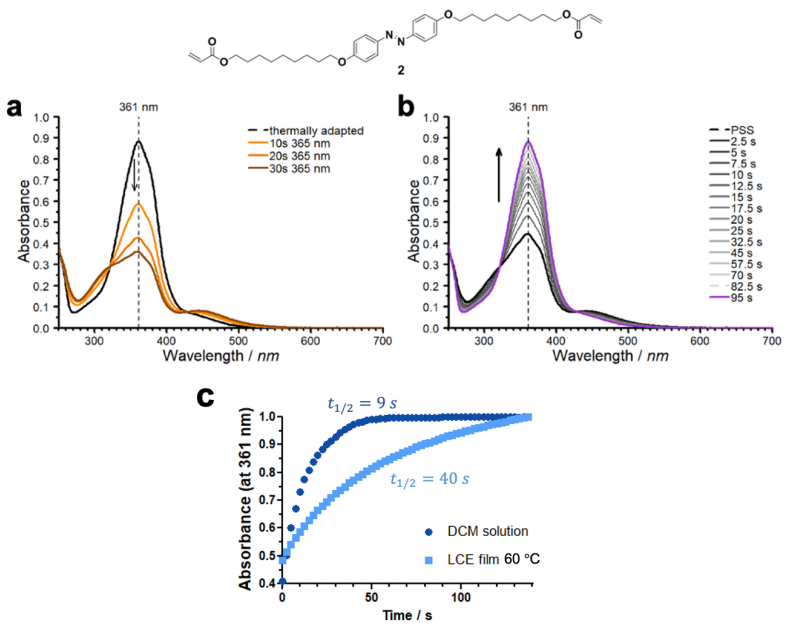

Supplementary Figure 5 | Representative absorption spectra for the photoisomerization of compound **2** (Synthon Chemicals, ST04181; λ_{max} = 361 nm, in dichloromethane; 293 K): **a.** Photoswitching from *trans*- to *cis*-isomer with 365 nm (ThorLabs, LED M365F1). **b.** Thermal relaxation from *cis*- to *trans*-isomer in the dark (PSS = photostationary state). **c.** Determination of the thermal half-life of the *cis*-isomer for compound **2** in dichloromethane (DCM) solution (as shown in part **b**) and in an LCE film at 60 °C: points correspond to measured data (observed at λ_{max} = 361 nm). The thermal half-life of the *cis*-isomer was determined to be $t_{1/2}$ ~9 s in dichloromethane solution and $t_{1/2}$ ~40 s in an LCE film at 60 °C. As one can tell from the comparison of the two, the thermal *cis*-to-*trans* relaxation rate strongly depends on the local molecular environment; dichloromethane as solvent was chosen for solubility.

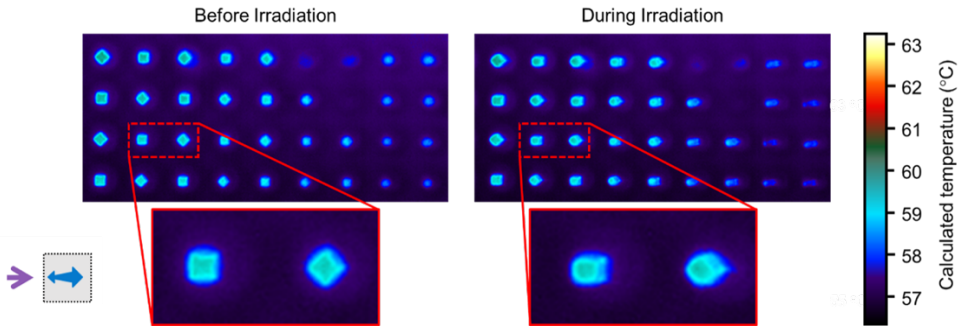

Supplementary Figure 6 | Thermal IR still images (FLIR A8303sc with 4x microscopy lens) of LCE microstructures with oblique-aligned LCE director on a heating stage set to 60 °C before and during in-plane UV-irradiation (115 mW/cm^2, M365F1 LED) from the left. No considerable photothermal heating is observed, which supports the notion that azobenzene crosslinker **2** mostly operates *via* photomechanical contraction[13–15]. Because of the IR camera, the UV LED to sample distance was in this case more than usual.

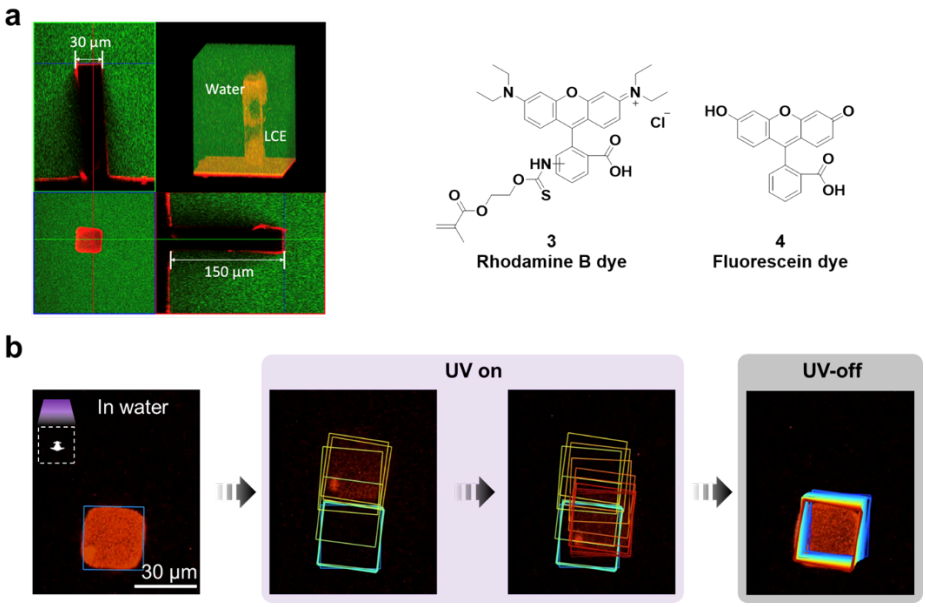

Supplementary Figure 7 | a. Z-stack of a square LCE micropost with oblique-aligned director orientation immersed in water. The image was obtained by confocal laser scanning microscopy (Zeiss, LSM700) with an immersion objective lens (Zeiss, W Plan-Apochromat 40x/1.0 DIC M27). The micropost was coated with Rhodamine B methacrylate **3** (shown in red, excited with λ_{ex} = 555 nm) and the aqueous layer dyed with fluorescein **4** (shown in green, excited with λ_{ex} = 488 nm). Note that water wets the microstructured surface well. **b.** Water acts as an effective heatsink and should thus suppress photothermal effects[13–15]. UV-actuation (at 115 mW/cm^2, Thorlabs M365F1) depicted as still frames and image-tracked traces (petrol to red = UV on and red to blue = UV off) show a similar actuation path as in air (a non-monotonic light-seeking as expected for small θ). The sample was kept on a heating element set to 65 °C. The observed deformation was recorded with the fluorescein channel disabled. Despite water dissipating any local photothermal heating, significant deformation was seen which further confirms that the azobenzene crosslinker **2** does not operate *via* a photothermal actuation mechanism.

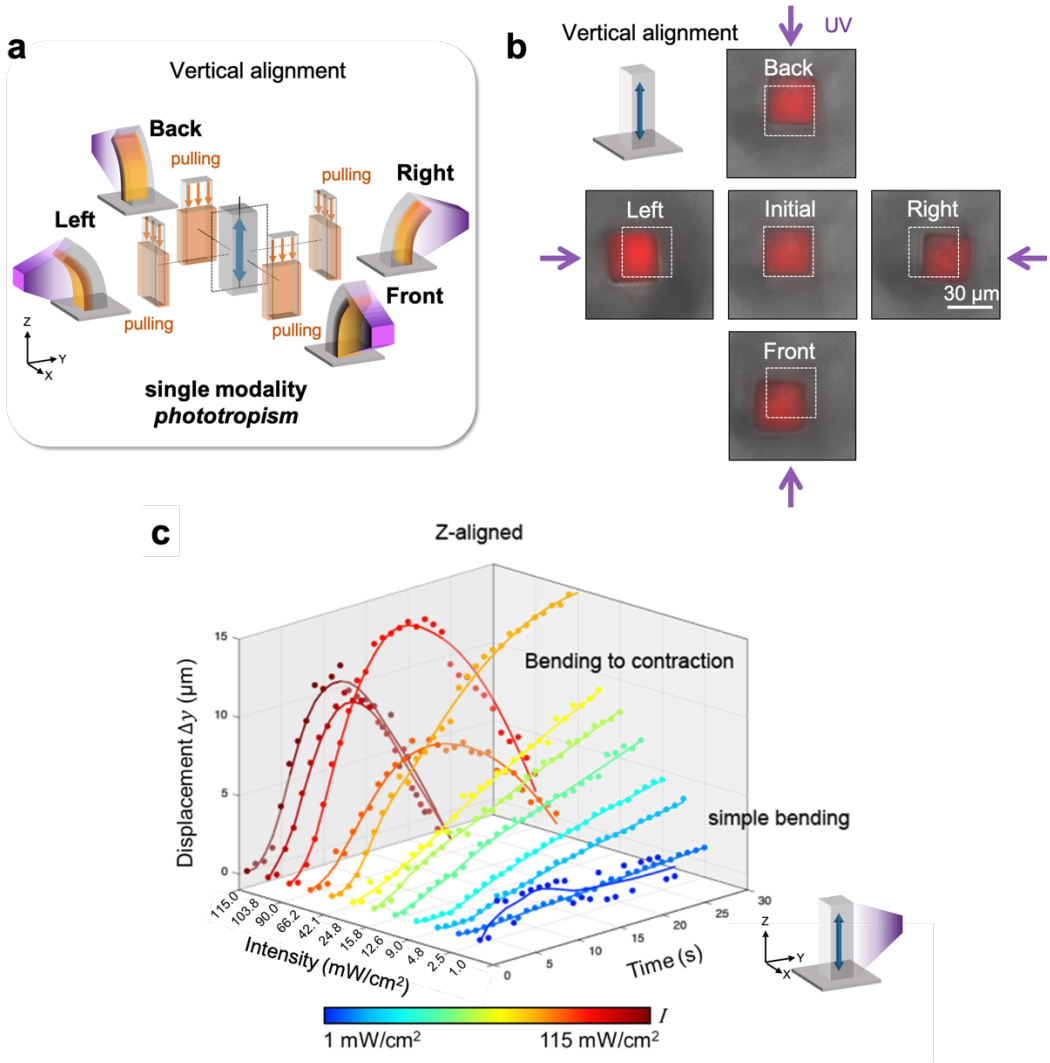

Supplementary Figure 8 | With an alignment along the principal symmetry axis, Z-alignment, only a single type of deformation—bending towards light—is expected, reminiscent of phototropism in nature[16]. **a.** Explanatory scheme to illustrate the origin of the observed phototropism: irrespective from what side the post is irradiated, in all cases the activated region at the irradiated face contracts along the Z-axis (illustrated with orange slabs), pulling on the 'non-activated' part (grey) and thus leading to bending towards light. **b.** Still frames from Supplementary Video **1** show 'light-seeking' deformation for UV-illumination from all four directions (back, right, front, and left; Thorlabs M365F1 at 15 mW/cm^2). Posts were stained with methacryloxyethyl thiocarbamoyl rhodamine B (**3**, shown in red, excited with λ_{ex} = 555 nm) for tracking *via* confocal fluorescence laser scanning microscopy. **c.** Quantification of photoactuation of a Z-aligned micropost under twelve different light-intensities ranging from 1 to 115 mW/cm^2 (1.0, 2.5, 4.8, 9.0, 12.6, 15.8, 24.8, 42.1, 66.2, 90.0, 103.8, and 115.0 mW/cm^2). Under the low to medium intensity regime (1.0 to 42.1 mW/cm^2, blue to light orange in the diagram), the microposts exhibit a bending deformation towards the light source (light-seeking) with increasing amplitude as the UV intensity increases. As the intensity continues to increase (66.2 to 115.0 mW/cm^2), a non-monotonic motion is observed, that constitutes initial light-seeking followed by reversal of bending direction to end up in a vertical, Z-contracted state, as governed by the director orientation. For more details on the image tracking, please refer to SI section 1.2.2.

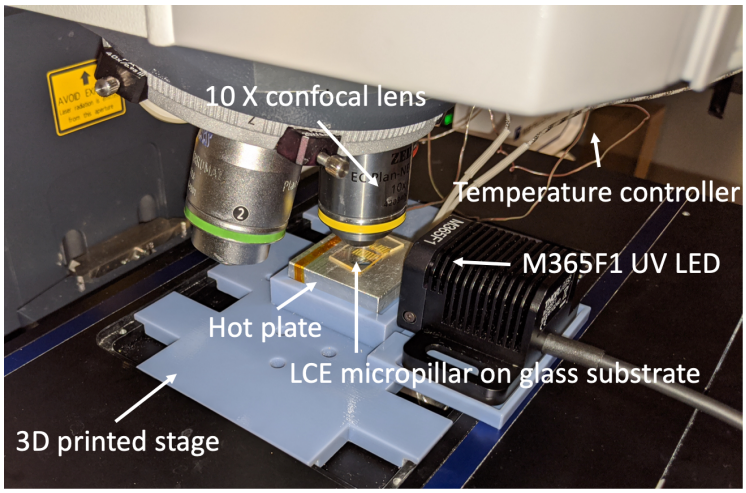

Supplementary Figure 9 | Custom-made imaging setup for confocal laser scanning microscopy comprising a 3D-printed sample stage, a temperature-controlled heating plate and slots to place the UV LED (Thorlabs M365F1). The LCE microstructures were heated to 60-70 °C (above their glassy state, T_g ~45 °C) for photoactuation with a UV LED.

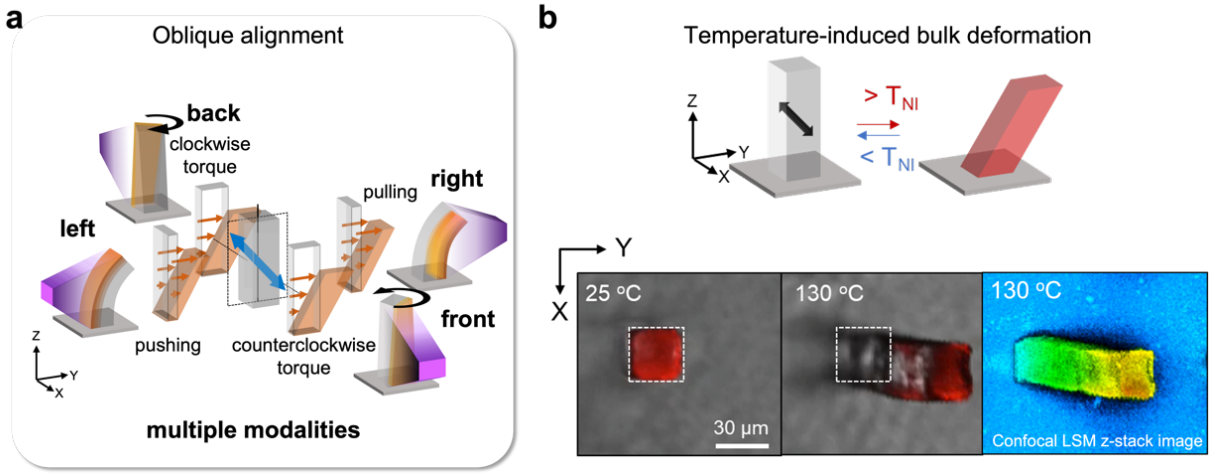

Supplementary Figure 10 | a. Upon breaking symmetry by tilting the director alignment away from the micropost principal symmetry axis to an oblique alignment, a multitude of deformations (light-seeking, light-avoiding, and twisting clock- and counterclockwise) are observed. The explanatory scheme illustrates the origin of the observed deformation behavior: all deformations are a result of the director-determined shearing to the right of the activated region (illustrated with orange slabs), which exerts different forces (pulling/pushing, orange arrows) and torques (clockwise/counterclockwise, orange arrows) on the 'non-activated' part (grey) of the micropost that depends on the facet of the structure being illuminated. Please also refer to Manuscript Figure **2** and Supplementary Video **1**. **b.** Characteristic bulk shearing deformation of LCE microposts to the right with tilted (oblique) molecular alignment when heated above the nematic-to-isotropic transition temperature (T_{NI}, Supplementary Figure **4**) at isotropic phase: A heating cycle (from 25 °C to 130 °C and back to 25 °C) confirms oblique bulk director alignment for the LCE square micropost, as above T_{NI} at isotropic phase, a clean thermal deformation (tilting) is observed. Posts were stained with methacryloxyethyl thiocarbamoyl rhodamine B (**3**, shown in red, excited with λ_{ex} = 555 nm) for tracking and 3D scanning (z-stack) *via* confocal fluorescence laser scanning microscopy (LSM).

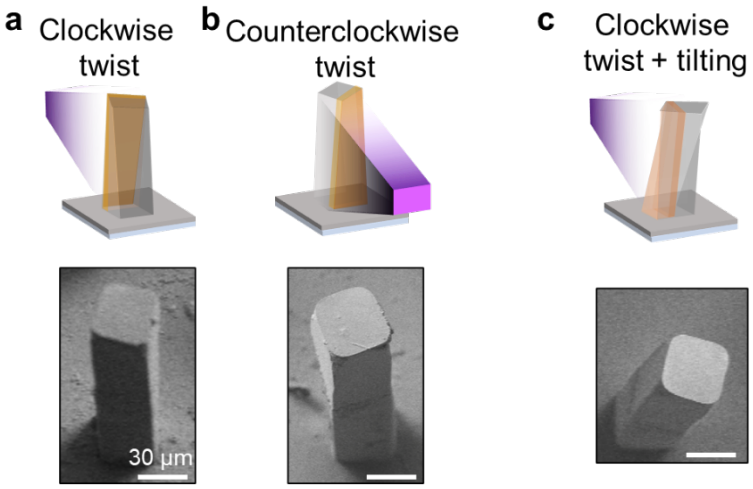

Supplementary Figure 11 | Kinetically trapped UV-deformed square microposts observed by field emission scanning electron microscopy (FESEM, Zeiss Supra 55 VP): **a-b.** low-intensity (15 mW/cm^2) UV illumination induced clockwise- and counterclockwise twisting (at 30° stage tilt), and **c.** medium-intensity (42 mW/cm^2) UV illumination triggered combination of clockwise twisting and tilting (at 15° stage tilt). The deformed LCE microposts were 'frozen' to fix the actuated shape in the glassy state of the LC elastomer by rapidly cooling from 60 °C to room temperature, which is below its glass transition temperature (T_g) of ~45 °C (Supplementary Figure **4**). The trapped LCE microposts were coated with 10 nm Pt/Pd (80:20) by sputter coating prior to imaging.

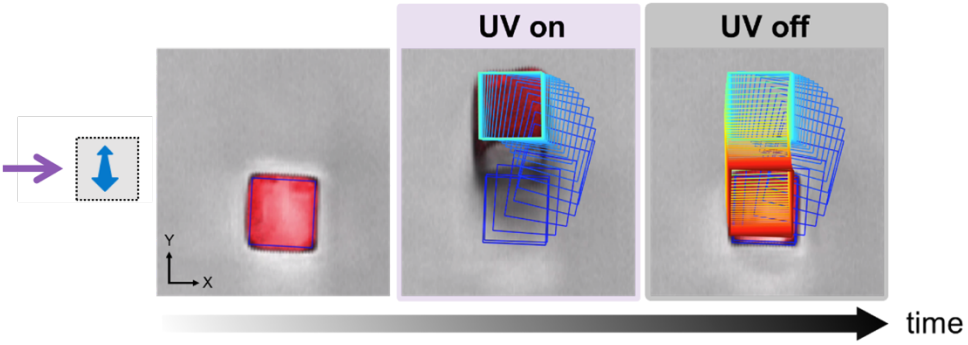

Supplementary Figure 12 | Example of image-tracking procedure: Fluorescent images used for image tracking (using a MATLAB script) and resulting fitted squares depicted as trace of a 'dancing' micropost (from blue to turquoise to orange). Each colored square corresponds to one fluorescent image. Note that in Manuscript Figure **3a** and Supplementary Figure **13** not all tracked squares are displayed for better visualization. For more details, please refer to SI section 1.2.2.

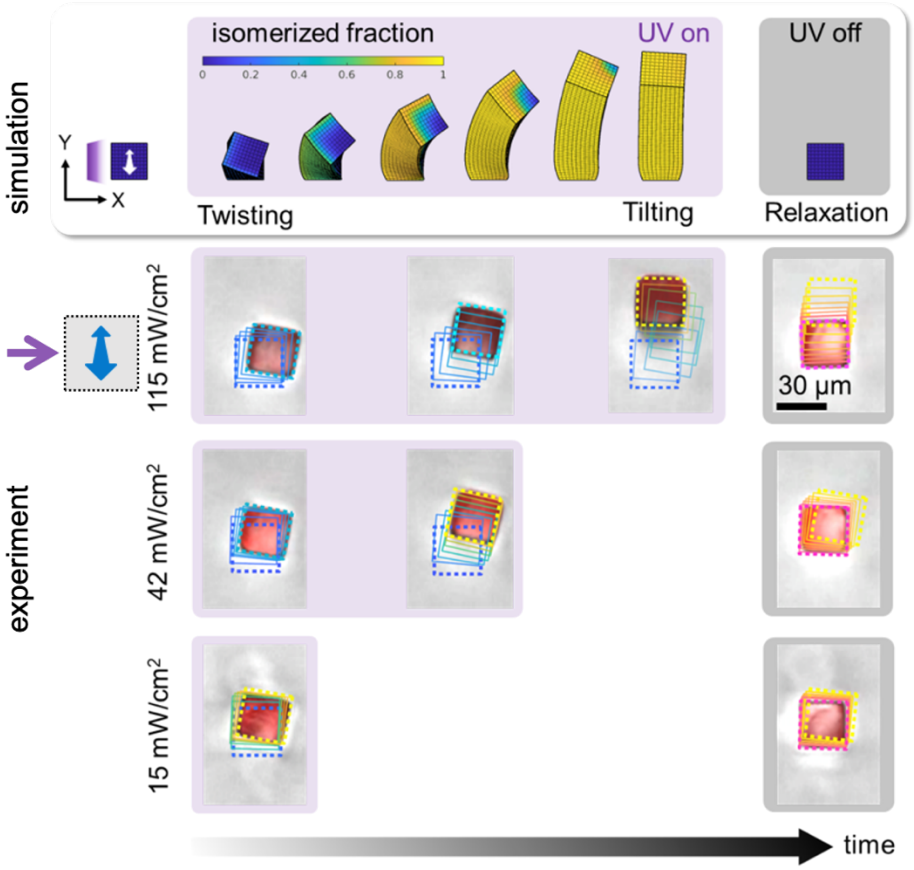

Supplementary Figure 13 | Comparison of simulated and experimental results demonstrating the characteristic non-linear motion trajectories of a micropost with oblique alignment and out-of-plane irradiation. UV-actuation at low (15 mW/cm^2), medium (42 mW/cm^2), and high (115 mW/cm^2) light intensity triggers non-linear deformation trajectories ranging from simple twisting to twisting and bending to 'dancing'. The still-frames are taken from Supplementary Video **2** with illumination along the X-axis. Stills of the finite element simulation are shown for comparison (Manuscript Figure **3a & b** and SI Section 2.1 for more details). Posts were stained with methacryloxyethyl thiocarbamoyl rhodamine B (**3**, shown in red, excited with λ_{ex} = 555 nm) for tracking *via* confocal fluorescence laser scanning microscopy.

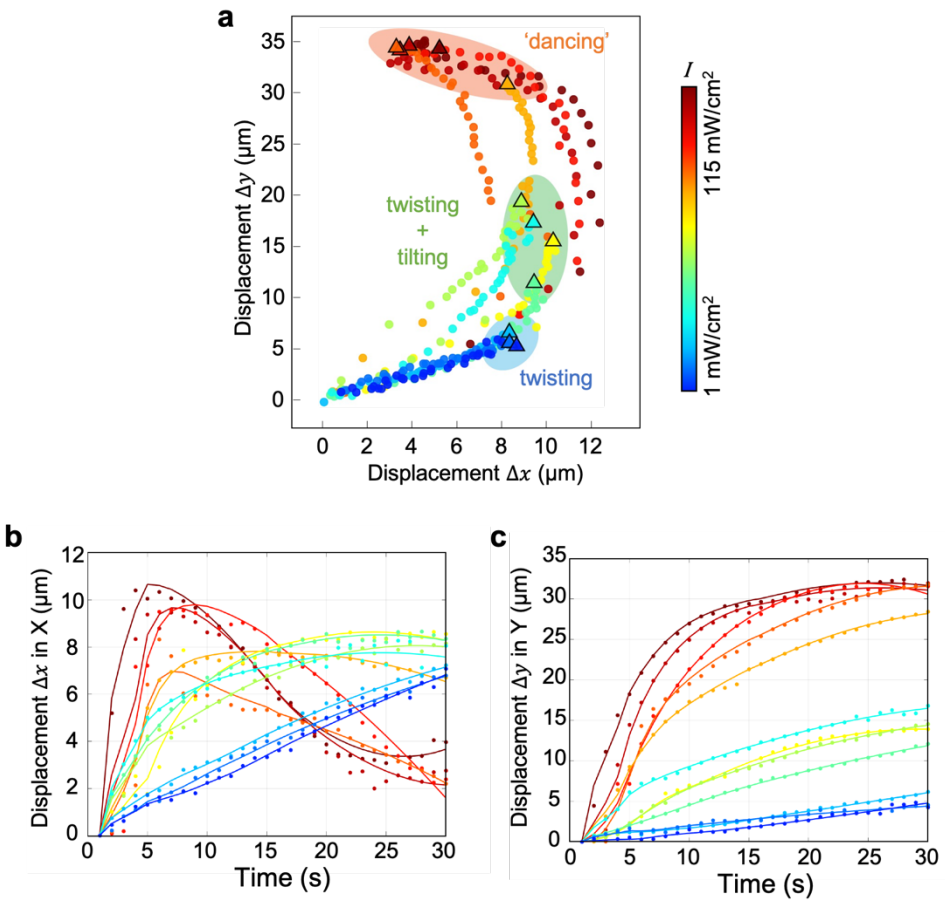

Supplementary Figure 14 | Quantification of the non-linear deformation trajectory of the micropost an oblique-aligned director (Manuscript Figure **3d**) with regard to the tip displacement along the X- and Y-axis for twelve different light-intensities ranging from 1 to 115 mW/cm^2 (1.0, 2.5, 4.8, 9.0, 12.6, 15.8, 24.8, 42.1, 66.2, 90.0, 103.8, and 115.0 mW/cm^2). **a.** Comparison of the elicited trajectories in the XY-plane; **b.** Corresponding time-traces for the displacement along the X-axis. **c.** Corresponding time-traces for the displacement along the Y-axis. As light intensity is increased, the maximum amplitude of post deformation (both in X and Y direction) is reached more quickly. For more details on the image tracking, please refer to SI section 1.2.2.

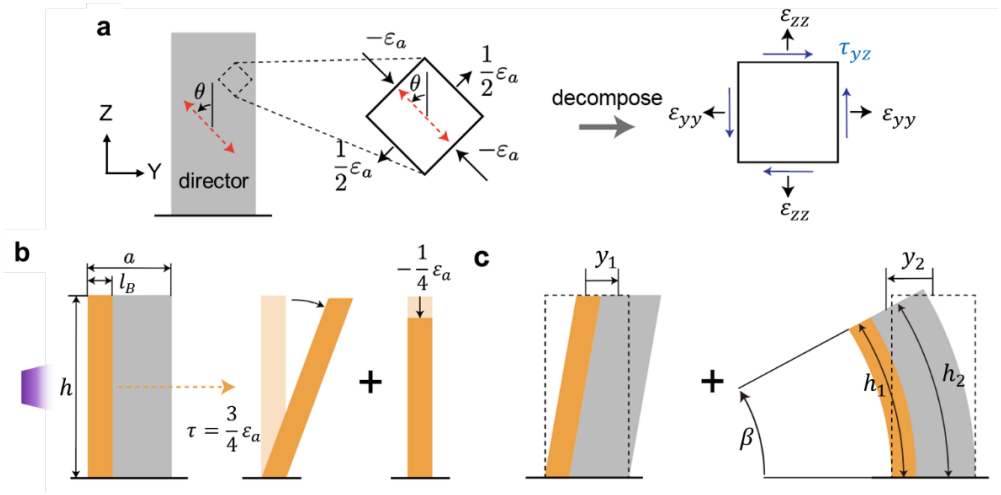

Supplementary Figure 15 | Theoretical model to explain the non-linear behavior for light-seeking and light-avoiding in microposts with oblique director alignment. **a.** Transformation of strain state from director frame to YZ frame to facilitate analysis. **b.** The deformation of the UV-actuated layer (depicted in orange) can be divided into two parts: shearing and contraction. **c.** The deformation of the 'activated' layer results in two different deformation modes of the entire post: shearing and bending. For more details, please refer to SI Model **2**, section 2.2.

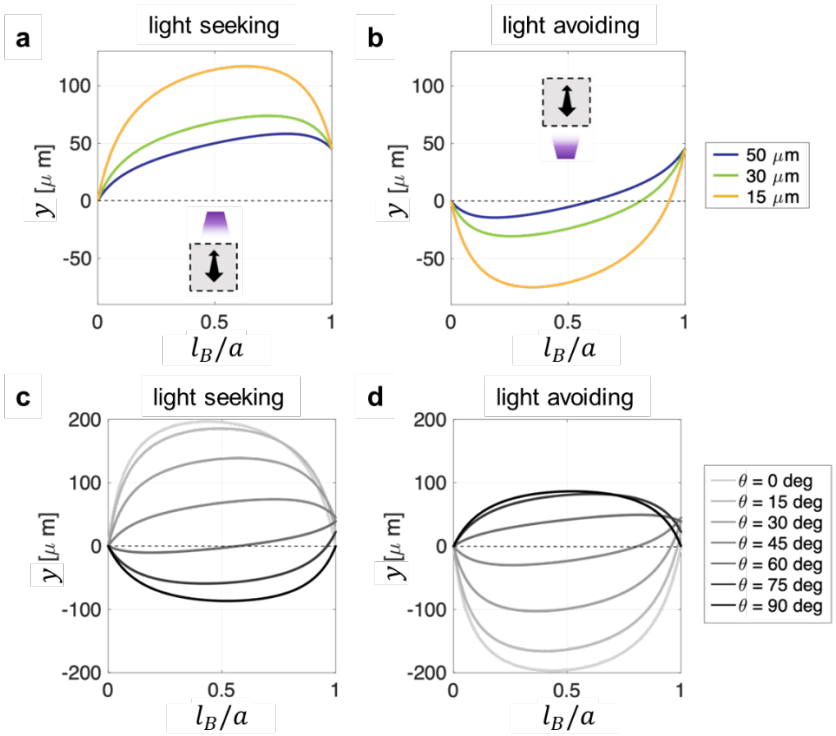

Supplementary Figure 16 | Theoretical model to account for the non-linear actuation behavior of microposts with oblique director alignment in the 'light-seeking' and 'light-avoiding' case (please refer to SI Model **2**, section 2.2 and Supplementary Figures **17-19**). **a-b**. Influence of post size (from 15 to 50 μm side length) on the tip motion of the micropost for 'light-seeking' (**a**) and 'light-avoiding' (**b**) behavior. **c-d**. Influence of director orientation (defined as director tilted at an angle θ away from Z-axis in the XZ-plane) on the tip motion of the post for **c**, 'light-seeking' (**c**) and 'light-avoiding' (**d**) behavior.

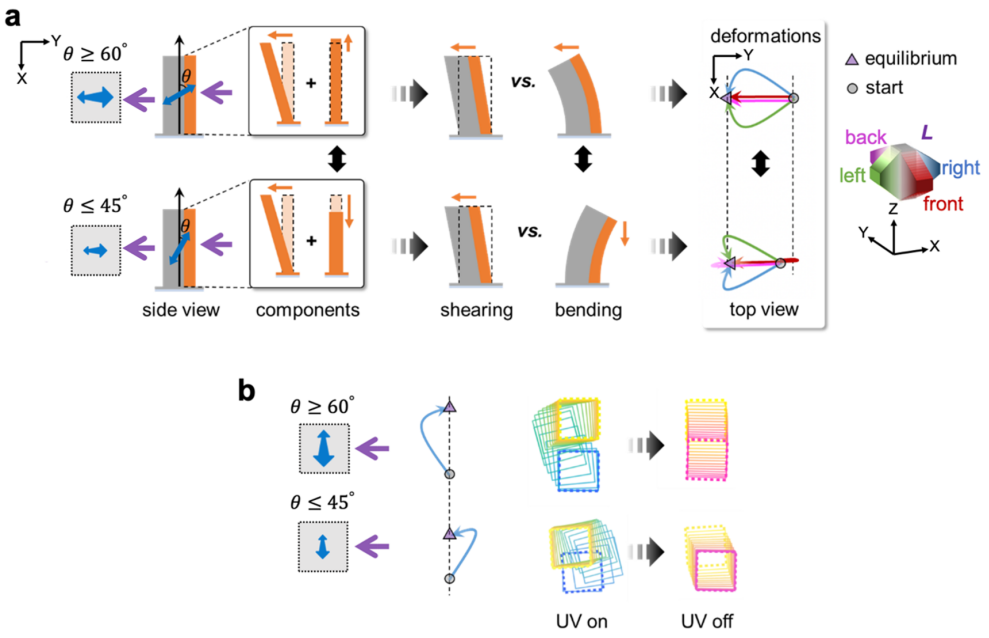

Supplementary Figure 17 | Effect of tilt of director orientation on deformation behavior of LCE microposts with oblique molecular alignment. While the final positions of the deformed posts under high-intensity UV-irradiation (115 mW/cm^2) are similar (identical to the deformed posts after thermal nematic-to-isotropic phase-transition, see *e.g.* Supplementary Figure **10b**), the deformation trajectories to that final sheared deformation state vary starkly depending on the tilt of the director alignment and the direction of illumination (Manuscript Figure **3e**): **a.** Deformations of the 'activated' layer for the oblique-aligned director contain two components, a shearing component (along the Y-axis) and a contracting/expanding component (along the Z-axis). A contraction along the Z-axis is expected for a director of $\theta \leq 45°$, whereas an expansion is expected for a director $\theta \geq 60°$. These opposite behaviors will lead to 'dancing' toward or away from the light source, respectively. Note the switch of the 'green' (irradiation from left) and 'blue' (irradiation from right) deformation trajectories for the two cases. The circle corresponds to the post starting position; the triangle denotes maximum displacement under irradiation. **b.** A change in director tilt causes a change from 'dancing away' to 'dancing towards' light for out-of-plane irradiation as the director alignment crosses a threshold between θ = 45°–60°. Tracked experimental deformation trajectories are depicted to illustrate these two types of behaviors.

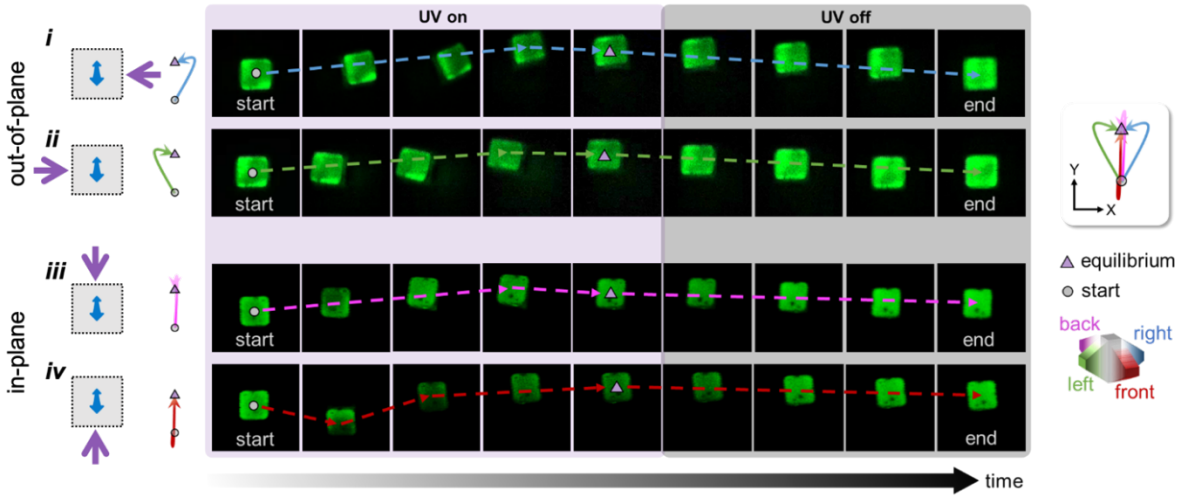

Supplementary Figure 18 | Confocal fluorescence laser scanning microscopy top-view still images depicting post deformations for UV-illumination from four directions *(i)* right, *(ii)* left, *(iii)* top, and *(iv)* bottom for the case of a molecular anisotropy tilted at $\theta \leq 45°$ (steep director orientation). Note that in the case of in-plane irradiation (*iii* & *iv*) the horizontal (pushing or pulling) and vertical (expanding) components may act either in a supportive (light-seeking case, *iii*) or in a counteractive fashion (light-avoiding case, *iv*) leading to pronounced reversal of deformation direction along the Y-axis. Posts were stained with methacryloxyethyl thiocarbamoyl rhodamine B (**3**, shown in green, excited with λ_{ex} = 555 nm) for tracking *via* confocal fluorescence laser scanning microscopy. For annotation, the circle corresponds to the post starting position; the triangle denotes maximum displacement under irradiation.

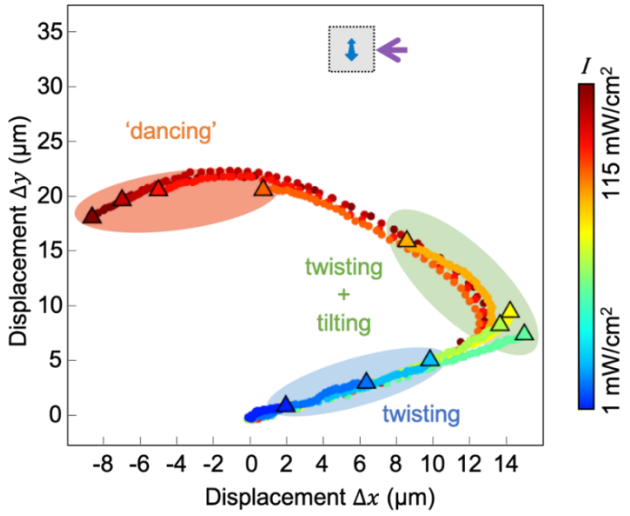

Supplementary Figure 19 | Quantification of the non-linear deformation trajectory of a micropost with a steeper oblique-aligned nematic director, tracing its displacement along the X- and Y-axes for eleven different light intensities ranging from 1 to 115 mW/cm^2 (1.0, 2.5, 4.8, 12.6, 15.8, 24.8, 42.1, 66.2, 90.0, 103.8, and 115.0 mW/cm^2). Note that the molecular director orientation is slightly titled out from the YZ-plane, which causes a displacement along the X-direction in the fully illuminated state. The extent of the final X-displacement can be programmed by controlling the director orientation in the XZ plane. For more details on the image tracking, please refer to SI section 1.2.2.

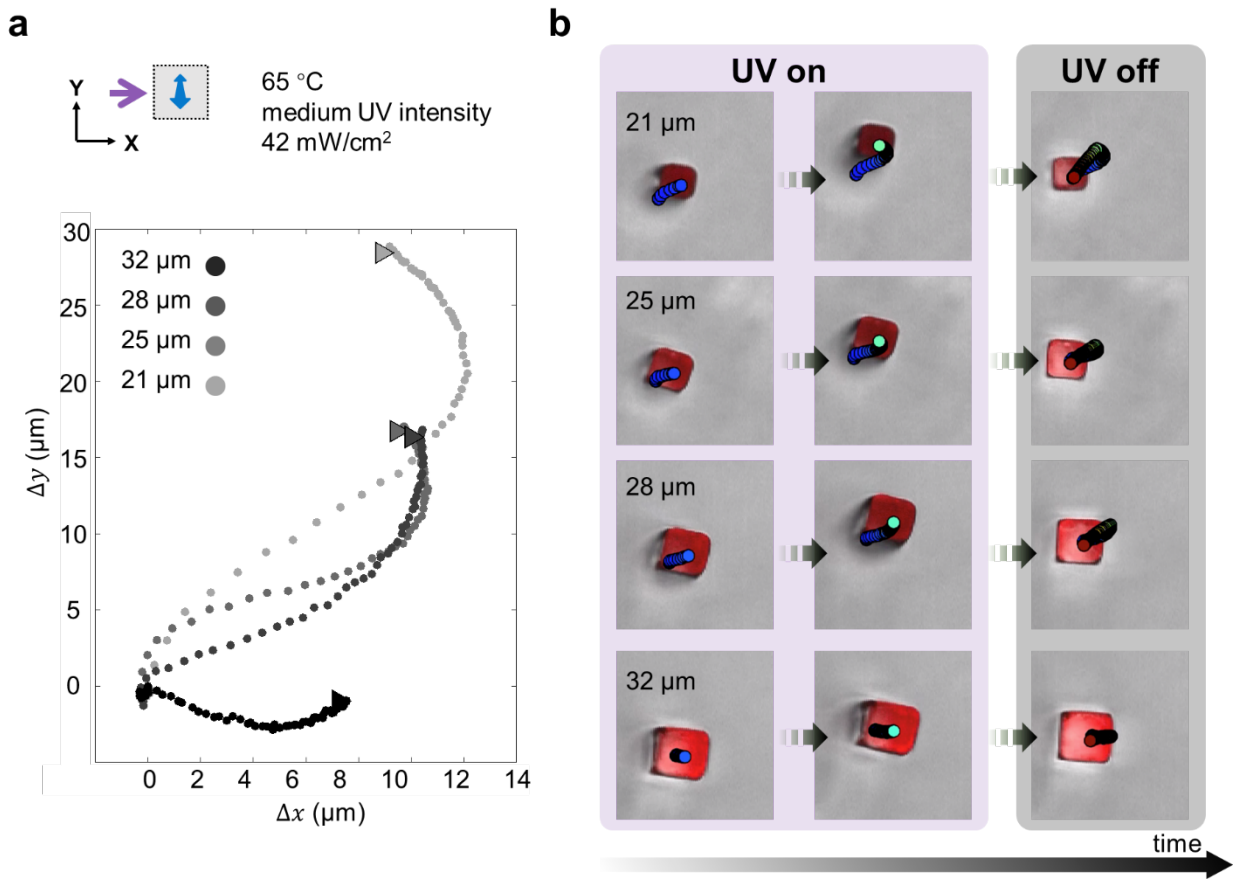

Supplementary Figure 20 | Quantification of the size-dependent deformation trajectories for microposts with oblique-aligned director ($\theta \geq 60°$) at medium light intensity (42 mW/cm^2). The deformation trajectory of LCE microposts of varying sizes (21, 25, 28, and 32 µm, respectively) changes drastically as a result of changes in bending stiffness and propagation dynamics of the traveling isomerization wave (Manuscript Figure **3f**). **a.** Deformation trajectories of the micropost tip obtained through image tracking. **b.** Confocal fluorescence laser scanning microscopy top-view still images for the four post thicknesses and overlayed imaged tracking for the center of the top face of the post. Pillars were stained with methacryloxyethyl thiocarbamoyl rhodamine B (**3**, shown in red, excited with λ_{ex} = 555 nm). See also Supplementary Video **4**.

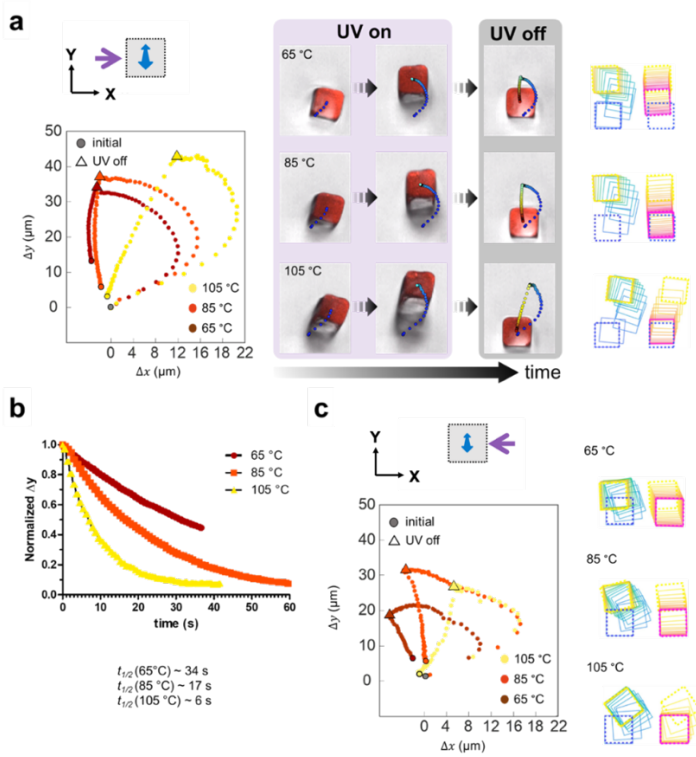

Supplementary Figure 21 | Quantification of the temperature dependence of deformation trajectories for microposts with an oblique-aligned director (Manuscript Figure **3g**). Under high-intensity (115 mW/cm^2) irradiation, increasing the temperature of the sample stage (from 65 °C to 105 °C) decreases material stiffness and speeds up the *cis*-to-*trans* thermal relaxation of the azobenzene crosslinker, reducing the photostationary state reached and restricting progression of the traveling isomerization front. As a result, deformations of obliquely aligned samples at 105 °C show larger initial amplitudes. **a.** Temperature-dependent behavior for flatter director tilt ($\theta \geq 60°$). **b.** Fitting of the normalized Y-displacement for the thermal recovery data presented in **a** with a single exponential process upon switching off the UV-irradiation ($t_{1/2}$ ~34s at 65 °C, ~17s at 85 °C, and ~6 s at 105 °C). **c**. Temperature-dependent behavior for a steeper alignment (closer to Z-alignment, $\theta \leq 45°$). See also Supplementary Video **4**.

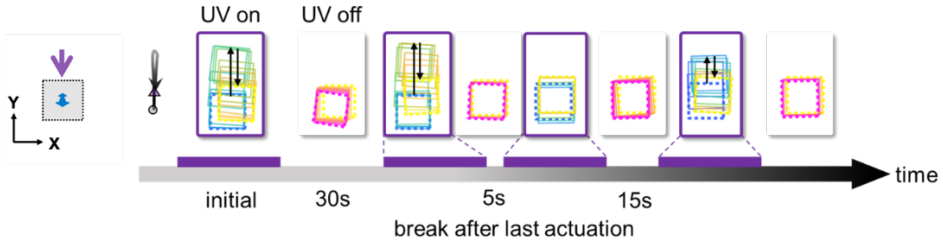

Supplementary Figure 22 | Refractory period observed in photoactuations: Image tracking of the deformations shown in Supplementary Video **5** for in-plane UV-irradiation of an oblique-aligned micropillar ($\theta \leq 45°$) submerged in water (to exclude any possible heating effects). Due to the non-instantaneous *cis*-to-*trans* thermal recovery of the photoswitchable crosslinkers, the ability of a pillar to undergo photoactuation directly after an excitation period is diminished as demonstrated with varying lengths of UV 'off' intervals in between UV 'on' periods. Also refer to Manuscript Figure **3h** for quantification of deformation amplitudes. The microposts were immersed in water throughout the measurement. A comparable behavior is observed also in air.

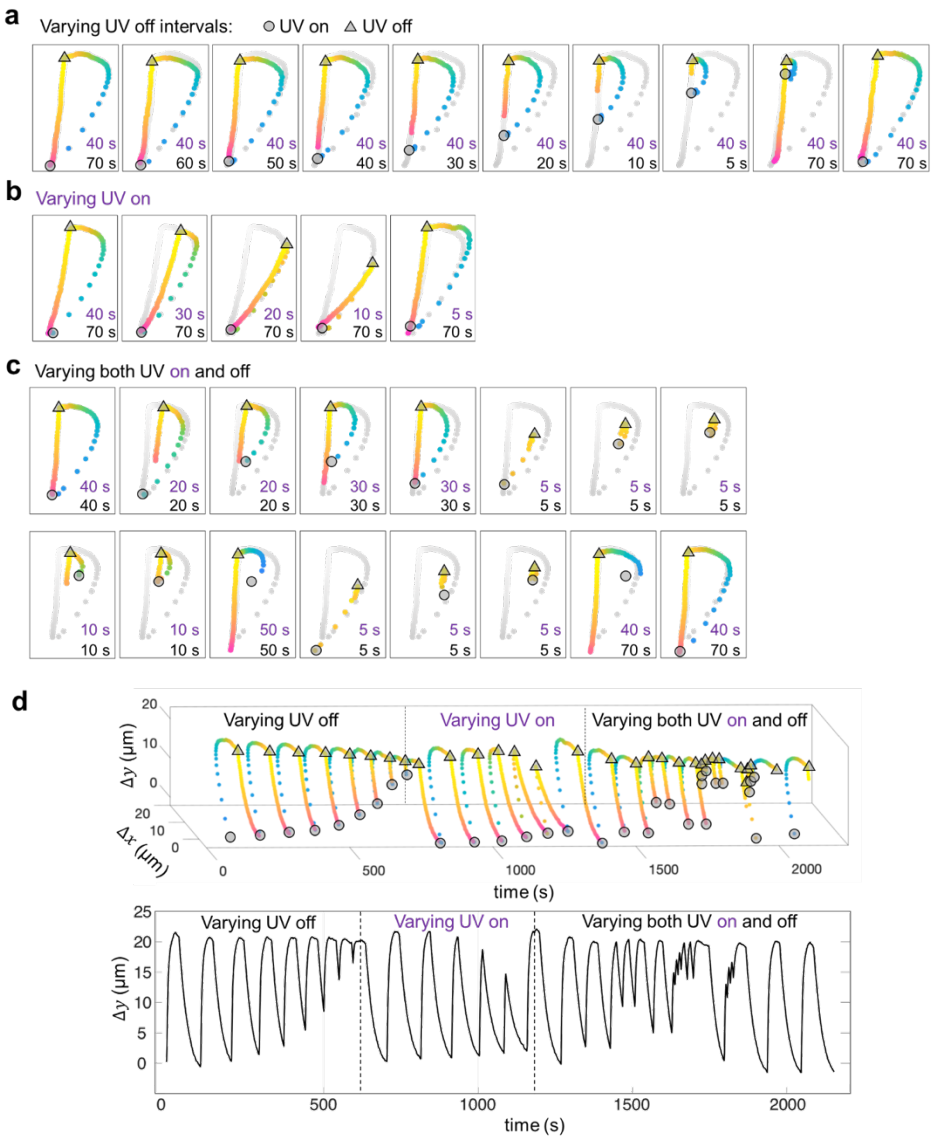

Supplementary Figure 23 | Deformation trajectories for a single oblique-aligned micropillar modulated by changing the (out-of-plane) irradiation on-off intervals at high light intensity (115 mW/cm^2), harnessing the effects of non-instantaneous thermal relaxation of the *cis*-azobenzene population as illustrated in Supplementary Figure **22**. **a.** For cycles of out-of-plane irradiation, when the UV irradiation times are kept constant, but relaxation times are gradually shortened, the final position of the pillar remains the same, but the starting position of each cycle moves towards the tilted state. Full amplitude actuation was resumed after complete relaxation (UV off 70 s). **b.** In contrast, when the relaxation time is kept constant, but UV irradiation times are consecutively shortened, the starting position remains the same, but the end position moves along the trajectory at full amplitude. Triangles denote maximum post displacement before switching the UV-irradiation off. **c.** Both the starting and end positions can be tuned by varying the irradiation on and off intervals. **d.** 3D traces of the photoactuation paths along both X- and Y-directions as a function of time for actuation pathways in **a**-**c**, top row, and 2D traces of the Y-displacement as a function of time, bottom row, illustrate the dynamic and highly programmable deformation behaviors (Supplementary Video **5**).

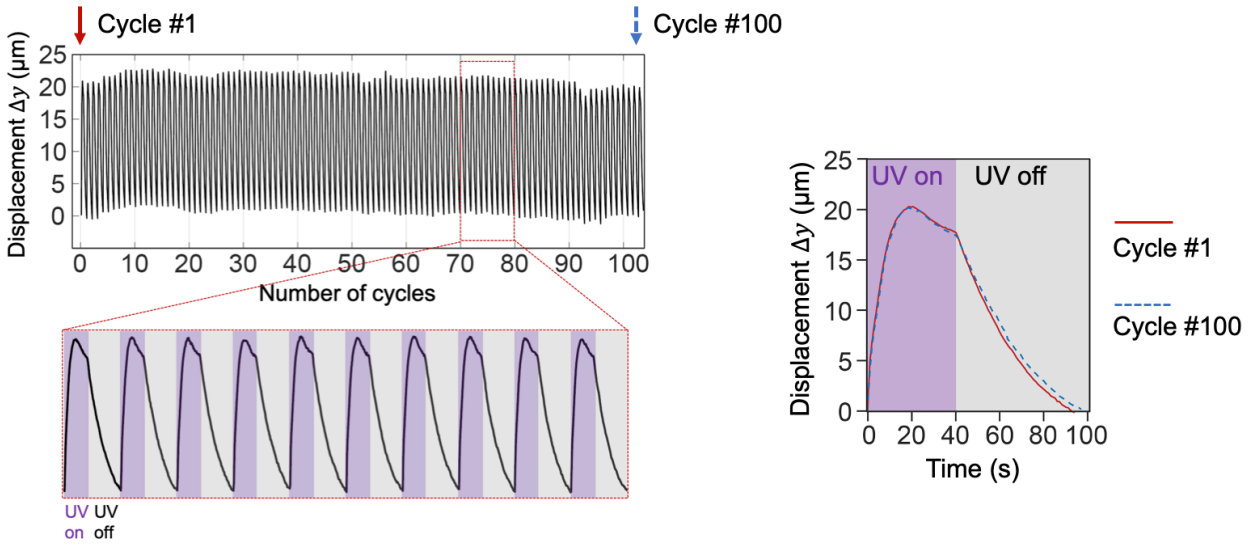

Supplementary Figure 24 | No appreciable fatigue is observed over at least 100 consecutive cycles of photoactuation at 115 mW/cm^2 for the example of out-of-plane 'dancing' behavior with UV 'on' 40 s and UV 'off' 60 s in each cycle at 60 °C. These results indicate that photodegradation effect is insignificant under the conditions studied.

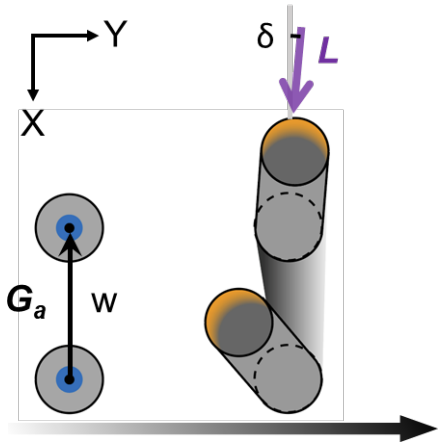

Supplementary Figure 25 | Schematic illustration of the origin of pattern formation in arrays of Z-aligned microposts (Manuscript Figure **4a**): Under experimental conditions that favor stable bimorphs, even a small misalignment between $\boldsymbol{G_{array}}$ and ***L*** causes symmetry breaking that can lead to starkly different deformations of posts along the array. As the first post bends towards the light along ***L*** with a small angle δ to the array axis $\boldsymbol{G_{array}}$, the subsequent post gets exposed to light only partially, promoting its out-of-plane bending, which gets amplified, the more the post deforms. The resulting location-dependent symmetry-breaking and deformation creates stable, self-organized patterns along the post array. Note that the velocity of propagation of the order-to-disorder front within each pillar can be different from the velocity of deformation along the array.

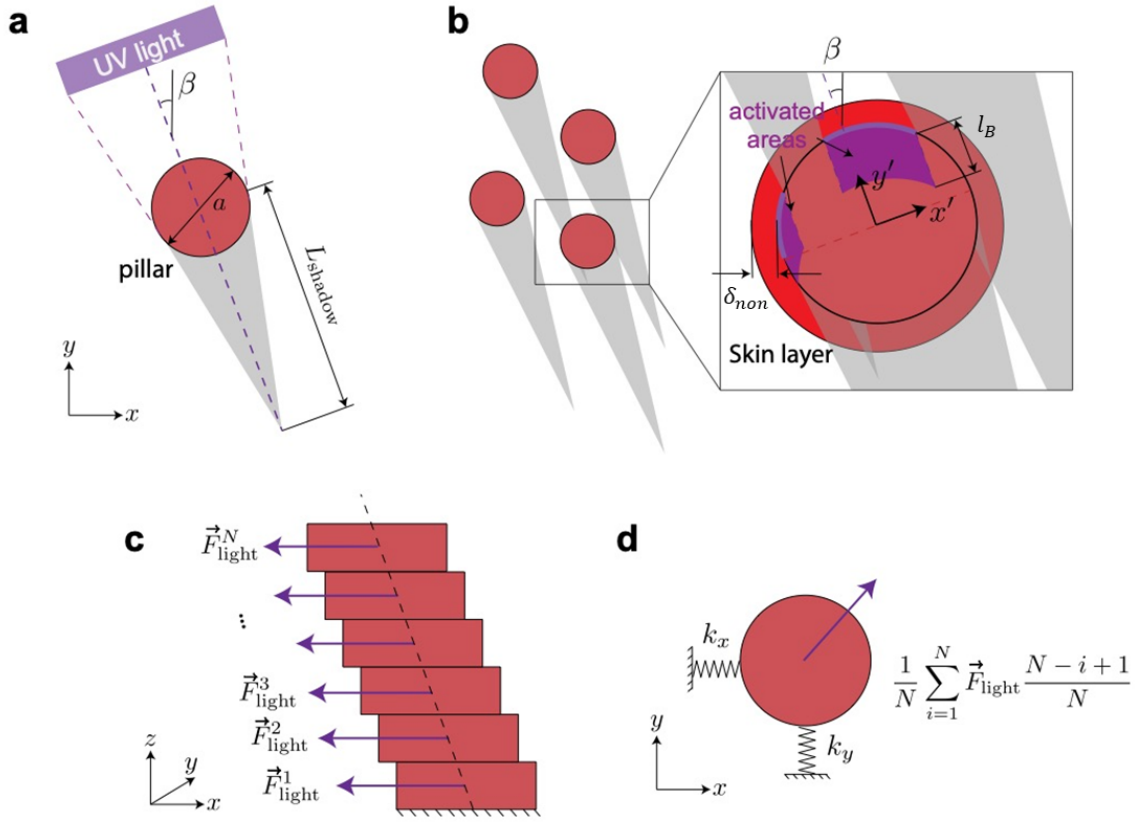

Supplementary Figure 26 | Discrete model to capture the collective deformation response of micropost arrays under UV light from different angles. **a.** The cylindrical post shades a triangular shadow against the UV light. **b.** For each post, the shadow from other posts blocks UV light. As a result, only part of the post is activated, considering penetration depth l_B and a ring of non-excitable material given by δ_{non}. **c.** We discretize the post as a stack of disks and each layer exerts an equivalent light-induced activation force. **d.** The total force is balanced by two linear springs to yield the final top displacements of the posts. For more details, please refer to SI Model **3**, section 2.3.

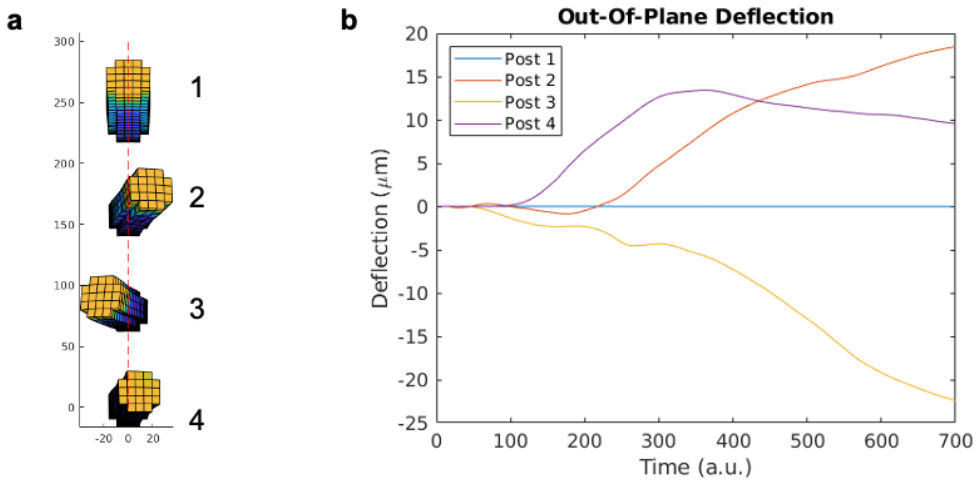

Supplementary Figure 27 | Simulated deformation of circular microposts within an array (Supplementary Video **6**). Posts are subject to irradiation from two light sources offset by ±1° offset to the array axis. Post dimensions correspond to a height of 150 μm and diameter of 30 μm, with a center-to-center separation of 78 μm along the array. **a.** The nematic director is oriented along the vertical (Z-)axis of the posts, resulting in phototropic bending. Light vectors are propagated through the finite elements as described in Model **1**. **b.** Out-of-plane (out-of-string) deformation through time for the four posts.

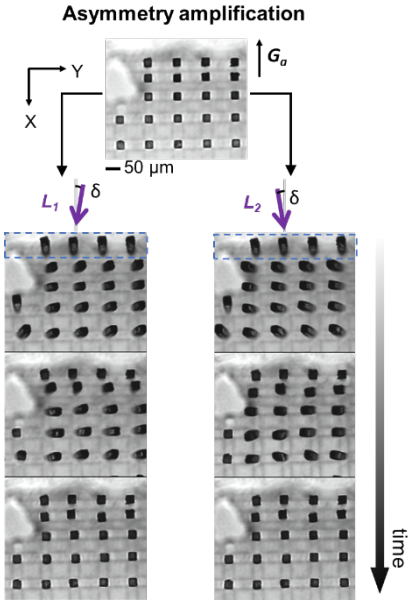

Supplementary Figure 28 | A clear asymmetry amplification effect is observed in an array of square microposts with mesogenic alignment along the Z-direction: for the same array, when light is along the X-axis with just a small negative/positive angle δ with regard to the X-axis (corresponding to G_a), amplification of the asymmetry is observed as the amplitude of out-of-plane deformation increases along the array. As δ is very small, no noticeable difference in light-seeking deformation is observed for first row of posts (marked with a blue dashed box). However, subjacent rows of posts are exposed to light asymmetrically because of interpost communication, amplifying the deformation out of plane. Temperature 60 °C.

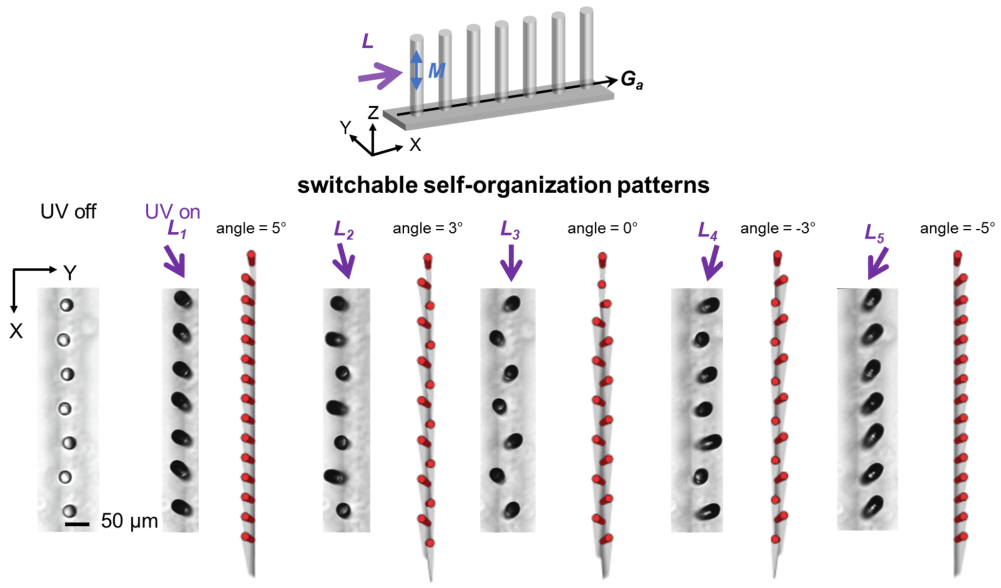

Supplementary Figure 29 | Variation of the angle of irradiation ***L*** with respect to G_a, creates different self-organized patterns of deformations under experimental conditions that favor stable bimorphs. While L_1 and L_5 show near-uniform out-of-plane bending (compare to the amplification observed in Supplementary Figure **28**), undulating wave-patterns of different accentuation are formed for angles associated with L_2, L_3, and L_4. The angles of purple arrows are exaggerated for illustration purposes. Formation of such wave-like patterns is highly reproducible. See also Supplementary Video **6**.

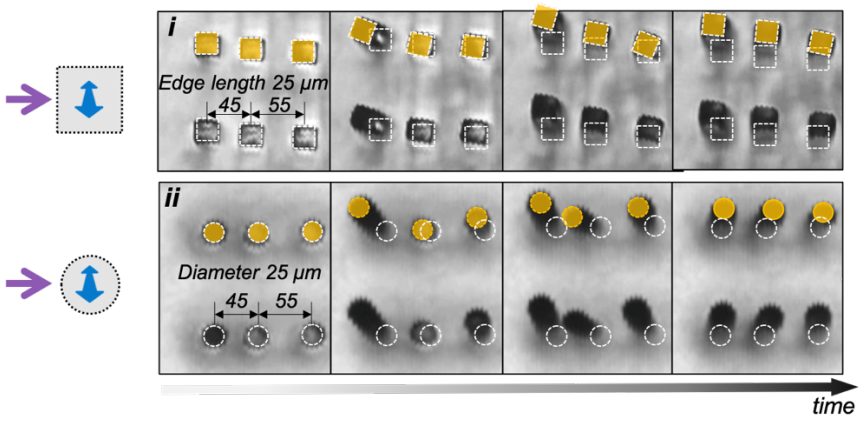

Supplementary Figure 30 | Spacing-dependent interpost communication in arrays of microposts of square and circular shape with an oblique director orientation, under conditions that allow for dynamic bimorph propagation (60 °C). In strings of posts with an array axis G_a orthogonal to the oblique director alignment ***M*** with variable interpost spacings (increasing from 45 µm to 55 µm and larger), strong coupling between posts located in close proximity is observed. Experimental still images demonstrate that when irradiated along the row of microposts, the post closest to the light source undergoes the characteristic non-linear 'power stroke' trajectory, while the post shadowed by the first starts moving with a time-delay, once the first post bends out of the way. Due to the presence of the first post only part of the second post is exposed to light and hence its 'power stroke' differs from the first.

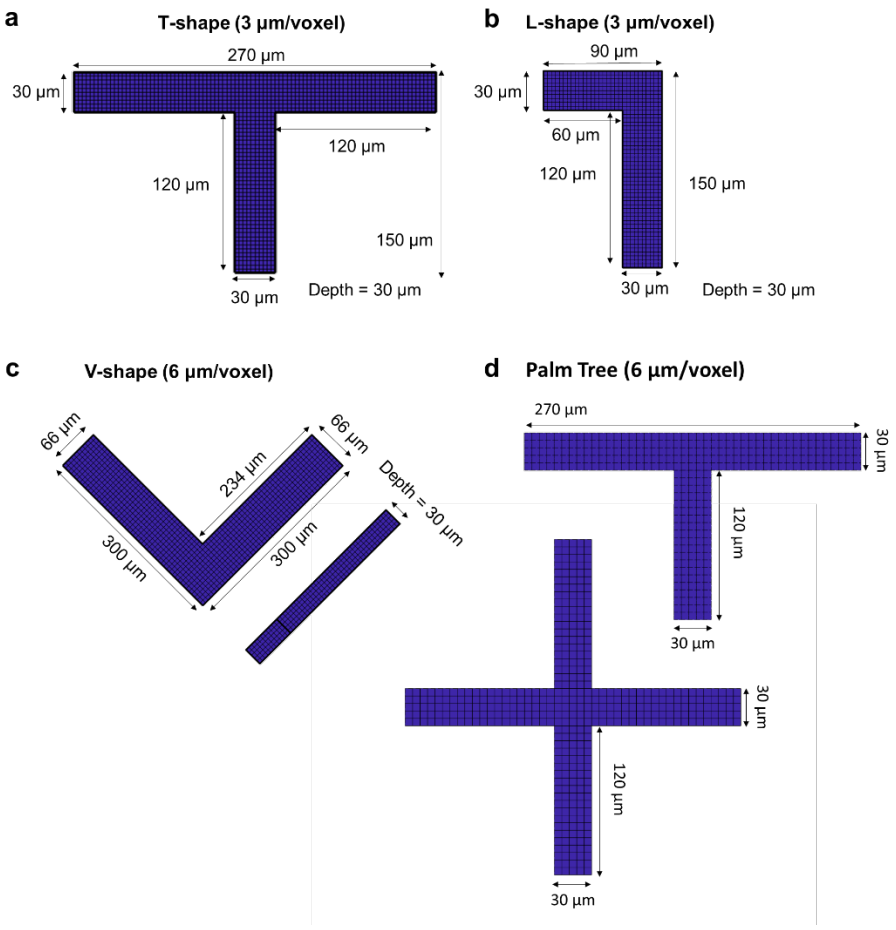

Supplementary Figure 31 | Dimensions of the simulated **a.** T-shaped, **b.** L-shaped, **c.** V-shaped, and **d.** Palm-tree-shaped structures discussed in Manuscript Figure **5b**. Code units were chosen to correspond to a resolution of one finite element voxel per 3 µm in **a & b** and per 6 µm in **c & d**.

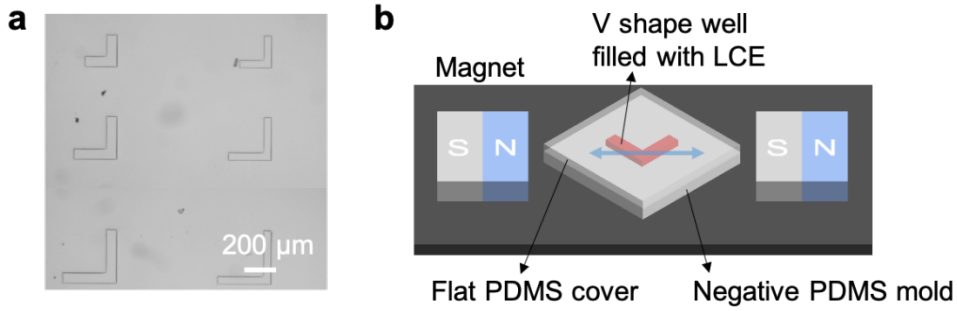

Supplementary Figure 32 | a. Optical micrograph of the PDMS mold with 'V' shape patterns of different dimensions: 75 x 200, 50 x 200, 75 x 300, 50 x 300, 75 x 400, and 50 x 400 µm (from top-left to bottom-right). All 'V' shaped jointed microstructures are 70 µm in depth (calculated from the SEM tilted-view image of the corresponding silicon master). **b.** Schematic depiction of the experimental setup for the magnetic alignment of freestanding 'V' shape LCE actuator. The polymerization was conducted following the same procedure as shown in Supplementary Figure **3** and SI section 1.2.3-1.2.5.

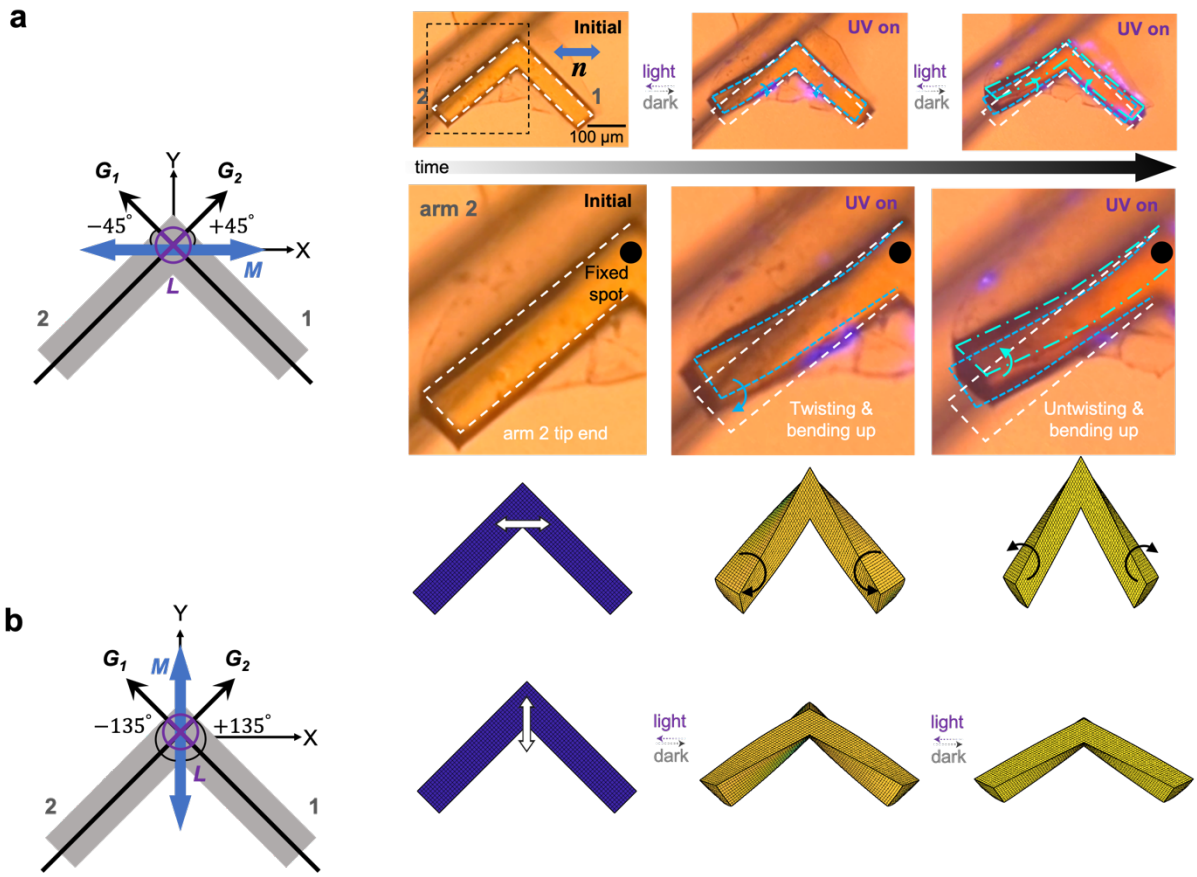

Supplementary Figure 33 | Freestanding single-material jointed V-shaped microstructures exhibit programmable twisting, bending, and shearing deformations. **a.** Design of a V-shaped LCE actuator containing two structural axes $\boldsymbol{G}_{\textbf{segment-1}}$ and $\boldsymbol{G}_{\textbf{segment-2}}$ (oriented along the two diagonals of the coordinate system). The structure has a uniform molecular alignment ***M*** along the X-axis, however the relative angles between ***M*** and the respective geometrical axes $\boldsymbol{G}_{\textbf{segment}}$ have opposite signs ($+45^{\circ}$ *vs.* -45°), which leads to opposite twisting and an overall closing motion (relative inwards shearing) of the two arms (segments) when illuminated along the Z-axis. As the light penetrates deeper into the thickness of the V-structure, the two arms begin to untwist, similar to what is observed in single microposts (Manuscript Figure **3a**). Top row shows experimental optical microscopic images. Zoomed-in images of arm **2** in the middle row show a clear twisting and untwisting along with upwards bending of the arm tip. Bottom row shows stills from the finite element (FE) simulation. Please also refer to Supplementary Video **9&10**. The black circle at the V-shape joint indicates the anchoring spot of the V-actuator to a capillary tube for hanging the structure in air. **b.** A V-shaped actuator with molecular alignment along the Y-axis (instead of X-axis) undergoes outwards twisting and opening of its two arms when illuminated along the Z-axis, as predicted by the FE simulation.

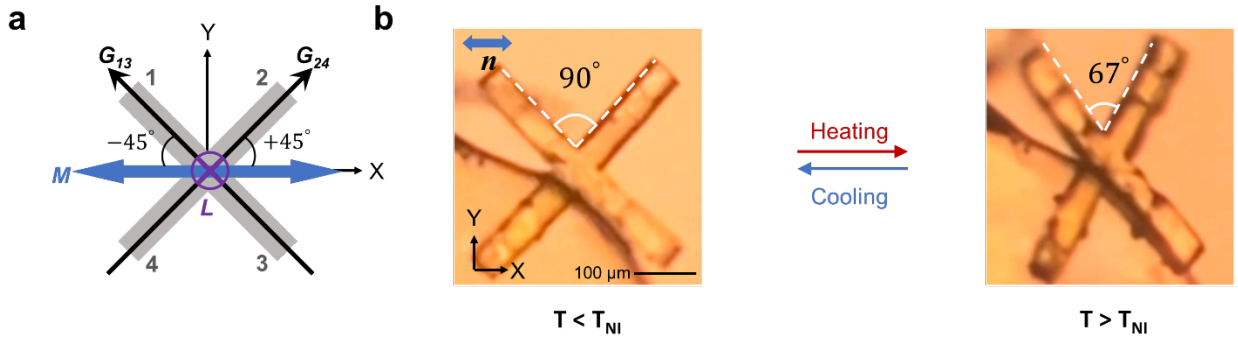

Supplementary Figure 34 | Freestanding jointed X-shaped microstructure with molecular alignment ***M*** along the X-axis (**a**) undergoes only shrinkage along the directorupon heating (from 25 °C to 130 °C and back to 25 °C), changing the X-shape to a 'slender' X-shape (**b**). Compare to the range of twisting, bending and shearing motions that the segments of the V-shape and X-shape display upon UV radiation (see Supplementary Figure **33** and Figure **5a** in the Main text).

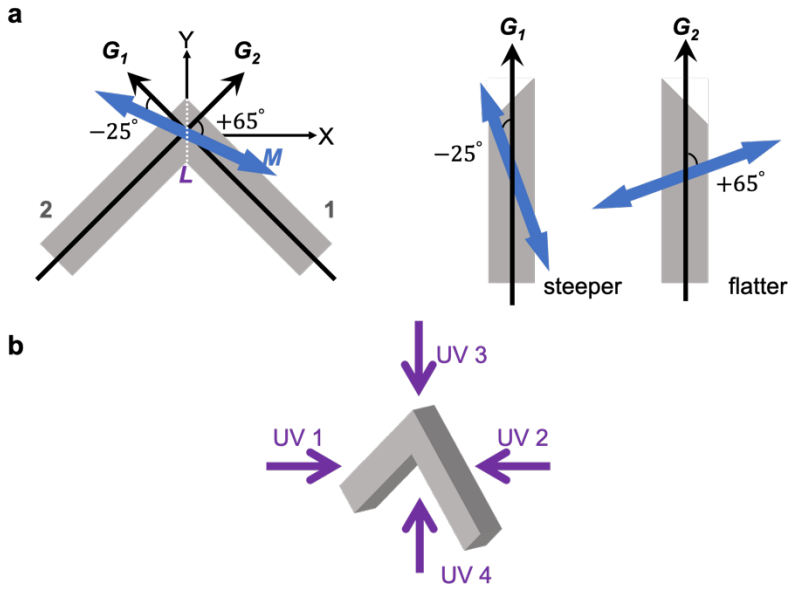

Supplementary Figure 35 | When the molecular alignment is offset with regard to the X-axis in a jointed microstructure of V-shape, the uniform bulk director orientation ***M*** forms different angles with $G_{segment}$, G_1 and G_2. As a result, these two segments (arms) exhibit different stroke-like deformations either toward ($\theta \leq 45°$) or away from the light ($\theta \geq 60°$) for out-of-plane irradiation (UV 1 and UV 2). Similarly, the arms will behave differently for in-plane irradiation (UV 3 & UV 4). Please also refer to Manuscript Figure **3e** for a detailed discussion on the influence of director tilt and different illumination directions in a square micropost on the post´s deformation behavior.

4 Supplementary Videos

Supplementary Video 1 | Single deformation mode *vs* multi-modal deformations under mild UV intensity (15 mW/cm^2). **Left:** Top view of light-responsive deformation of Z-aligned LCE square micropost exhibiting only one deformation mode – bending towards the light – for all illumination directions (see also Supplementary Figure **8**). **Right:** Top view of light-responsive deformation of LCE square micropost with oblique mesogen alignment exhibiting different deformation modes: clockwise twisting (irradiation from back), 'light-seeking' (irradiation from right), counterclockwise twisting (irradiation from front), and 'light-avoiding' (irradiation from left). Please also refer to Figure **2** in the main text and Supplementary Figures **10-11**).

Supplementary Video 2 | Light intensity-dependent self-regulated non-linear actuation. Qualitative agreement of experimentally observed and theoretically predicted (Finite Element simulations, SI section 2.1) micropost deformations for LCE microposts with oblique mesogen alignment irradiated out-of-plane at high- (115 mW/cm^2), medium- (42 mW/cm^2), and low- (15 mW/cm^2) light intensity. Simulation results were rescaled in time to match the experiment. Color scale corresponding to collective *trans*- (blue) to *cis*- (yellow) photoisomerization of the azobenzene cross-linker.

Supplementary Video 3 | Photoactuation of an LCE square micropost with oblique mesogen alignment illuminated from opposite directions at high light-intensity (115 mW/cm^2) results in mirrored stroke-like deformation trajectories.

Supplementary Video 4 | Effect of geometry and temperature on the light-responsive deformation of microposts with oblique mesogen alignment. **Top:** Top view of deformation trajectories for LCE microposts of different edge lengths (32, 28, 25, and 21 μm, from left to right) under medium light intensity (42 mW/cm^2) (Supplementary Figure **20,** Manuscript Figure **3f**). **Bottom:** Top view of deformation trajectories for LCE microposts actuated at different temperatures under high (115 mW/cm^2) irradiation intensities (Supplementary Figure **21**, Manuscript Figure **3g**).

Supplementary Video 5 | Effect of irradiation duration and intervals**. Left:** Top view of light-responsive 'light-seeking' deformation of LCE square microposts with steeper oblique mesogen alignment immersed in water (Supplementary Figure **22**) under in-plane irradiation at high light intensity (115 mW/cm^2) with varying time breaks in between actuation cycles (30s, 5s, then 15s). A reduction in deformation amplitude was observed with shorter time breaks in between two illumination periods (Manuscript Figure **3h**). **Right:** Top view of out-of-plane 'dancing' deformations of a photoresponsive oblique-aligned micropost modulated by changing the irradiation 'on'-'off' intervals at high light intensity (115 mW/cm^2). Depending on the duration of the interval of irradiation or relaxation, various starting and end positions can be sampled. Please refer to Supplementary Figure **23** for more details on lengths of UV-'on' and UV-'off' in each cycle.

Supplementary Video 6 | Self-sorted patterns appearing in microstructure arrays upon illumination through interpost communication. **Left:** Experiment and simulation of the self-organization of the array of closely packed microposts with Z-aligned mesogens into an undulating line. Note that $\boldsymbol{G_{array}}$ and $\boldsymbol{L}$ are slightly misaligned (by a small angle δ, Supplementary Figure **25**, Manuscript Figure **4a** & **b**). **Right:** Different self-organized patterns form by slightly changing δ. Note that indicated angles of illumination are exaggerated for illustration purposes (Supplementary Figure **29**).

Supplementary Video 7 | Spacing-dependent interpost communication in 2D pillar arrays. **Left:** In square 2D arrays, changing the illumination from the nearest-neighbor direction to diagonal influences the presence or absence of interpost communication and collective behavior (Manuscript Figure **4c**). **Right:** Irradiation of a circular array of microposts creates collective deformation dynamics, in which a global deformation front travels concurrently (with a different propagation velocity) across the array shaped by the locally changing interpost spacing and different $\boldsymbol{G_a}$-axes (Manuscript Figure **4d**).

Supplementary Video 8 | Amplification of 'defects' in arrays of microposts with oblique mesogen alignment: missing posts alter the interpost spacing and dramatically change the deformation trajectories of neighboring posts and thus the overall collective deformation dynamics (Manuscript Figure **4e**). Note the similar behavior of the 'effective first row' (denoted by red circles).

Supplementary Video 9 | Photoresponse of jointed microstructures. **Left:** A free-standing V-shaped jointed microstructure with a director alignment of +45° and –45° relative to the two respective segments (arms) exhibits simultaneous bending and twisting motions of opposite direction for the two arms (Supplementary Figure **33**). **Middle:** The directionality of these motions can be programmed through director orientation, as an X-shaped actuator (anchored at its center) demonstrates (Supplementary Figure **34**, Manuscript Figure **5a,*i***). **Right:** If an X-shaped actuator is anchored at the end of one segment, its twisting motion amplifies through the horizontal branching arm (Manuscript Figure **5a,*ii***).

Supplementary Video 10 | Simulation results of the photoresponsive behavior of L-, V-, T-, & palm-tree-shaped LCE microactuators (Supplementary Figure **31**) with horizontal, vertical, or oblique global director alignment exhibiting a range of non-trivial motions interesting for soft robotic applications.

5 References

1. Seebach, D., Imwinkelried, R. & Stucky, G. Optisch Aktive Alkohole aus 1,3-Dioxan-4-onen: Eine Praktikable Variante der Enantioselektiven Synthese unter Nucleophiler Substitution an Acetal-Zentren. *Helv. Chim. Acta* **70,** 448–464 (1987).
2. Fulmer, G. R., Miller, A. J. M., Sherden, N. H., Gottlieb, H. E., Nudelman, A., Stoltz, B. M., Bercaw, J. E. & Goldberg, K. I. NMR chemical shifts of trace impurities: Common laboratory solvents, organics, and gases in deuterated solvents relevant to the organometallic chemist. *Organometallics* **29,** 2176–2179 (2010).
3. Thomsen, D. L., Keller, P., Naciri, J., Pink, R., Jeon, H., Shenoy, D. & Ratna, B. R. Liquid crystal elastomers with mechanical properties of a muscle. *Macromolecules* **34,** 5868–5875 (2001).
4. Chandra, D., Taylor, J. A. & Yang, S. Replica molding of high-aspect-ratio (sub-)micron hydrogel pillar arrays and their stability in air and solvents. *Soft Matter* **4,** 979–984 (2008).
5. Zhang, Y., Lo, C. W., Taylor, J. A. & Yang, S. Replica molding of high-aspect-ratio polymeric nanopillar arrays with high fidelity. *Langmuir* **22,** 8595–8601 (2006).
6. Yao, Y., Waters, J. T., Shneidman, A. v, Cui, J., Wang, X., Mandsberg, N. K., Li, S., Balazs, A. C. & Aizenberg, J. Multiresponsive polymeric microstructures with encoded predetermined and self-regulated deformability. *Proc. Natl. Acad. Sci. USA* **115,** 12950–12955 (2018).
7. Gennes, P.-G. de. *The physics of liquid crystals*. (Clarendon Press , 1993).
8. Buguin, A., Li, M. H., Silberzan, P., Ladoux, B. & Keller, P. Micro-actuators: When artificial muscles made of nematic liquid crystal elastomers meet soft lithography. *J. Am. Chem. Soc.* **128,** 1088–1089 (2006).
9. Demus, D., Goodby, J. W., Gray, G. W., Spiess, H. W. & Vill, V. *Handbook of Liquid Crystals*. **2,** (Wiley-VCH, 2011).
10. Waters, J. T., Li, S., Yao, Y., Lerch, M. M., Aizenberg, M., Aizenberg, J. & Balazs, A. C. Twist again: Dynamically and reversibly controllable chirality in liquid crystalline elastomer microposts. *Sci. Adv.* **6,** eaay5349 (2020).
11. Corbett, D., van Oosten, C. L. & Warner, M. Nonlinear dynamics of optical absorption of intense beams. *Phys. Rev. A* **78,** 13823 (2008).
12. Beer, F. P., Johnston, E. R., DeWolf, J. T., Mazurek, D. F. & Sanghi, S. *Mechanics of materials*. (McGraw-Hill, 2020).
13. Gelebart, A. H., Vantomme, G., Meijer, E. W. & Broer, D. J. Mastering the photothermal effect in liquid crystal networks: A general approach for self-sustained mechanical oscillators. *Adv. Mater.* **29,** 1606712 (2017).
14. Gelebart, A. H., Jan Mulder, D., Varga, M., Konya, A., Vantomme, G., Meijer, E. W., Selinger, R. L. B. & Broer, D. J. Making waves in a photoactive polymer film. *Nature* **546,** 632–636 (2017).
15. Pilz da Cunha, M., van Thoor, E. A. J., Debije, M. G., Broer, D. J. & Schenning, A. P. H. J. Unravelling the photothermal and photomechanical contributions to actuation of azobenzene-doped liquid crystal polymers in air and water. *J. Mater. Chem. C* **7,** 13502–13509 (2019).
16. Page, R. M. Light and the asexual reproduction of pilobolus. *Science* **138,** 1238–1245 (1962).